Development of copper matrix composites reinforced by alumina and carbon materials via synergic milling

Adolfo José de Melo Chinopa de Sousa Ribeiro

Thesis to obtain the Master of Science degree in

Materials Engineering

Supervisors: Prof. Alberto Eduardo Morão Cabral Ferro
Prof. Ana Mafalda Saldanha Guedes

Examination Committee

Chairperson: Prof Maria Emília da Encarnação Rosa
Supervisor: Prof. Alberto Eduardo Morão Cabral Ferro
Member of the Committee: Prof. Daniela da Silva Nunes Gomes

October 2020

Declaration

I declare that this document is an original work of my own authorship and that it fulfils all the requirements of the Code of Conduct and Good Practices of the Universidade de Lisboa.

Declaração

Declaro que o presente documento é um trabalho original da minha autoria e que cumpre todos os requisitos do Código de Conduta e Boas Práticas da Universidade de Lisboa.

Agradecimentos

A conclusão desta tese apenas foi possível através do esforço conjunto de todas as pessoas que participaram na minha vida. Àqueles que me ajudaram, àqueles que me ensinaram, àqueles que me inspiraram e àqueles que tornaram a minha vida mais bonita.

Ao Professor Alberto Ferro, que me orientou, agradeço a os conhecimentos ensinados, o rigor que transmitido aos meus método e trabalho e os sermões merecidos.

Um obrigado especial à professora Mafalda Guedes, que coorientou esta tese, pelas longas que passou comigo a na obtenção dos resultados experimentais e pela sua ajuda na respectiva interpretação.

Um obrigado ao meu colega e amigo Miguel Costa por me ter ajudado, nas etapas iniciais da tese, com a orientação sobre o trabalho no laboratório, e noções gerais sobre a elaboração deste trabalho.

Um agradecimento à POMETON SPA, pelo fornecimento dos pós de cobre que serviram de base ao projecto.

Sem eles não conseguiria realizar este trabalho.

Um agradecimento especial ao meu professor de filosofia Jorge Saraiva e ao filósofo Slavoj Zizek, por me ajudarem a analisar o mundo e me transmitirem o amor pelo cinema.

Sem eles não desejaria realizar este trabalho.

Agradeço também aos meus pais, pela ajuda e o amor que me ofereceram desde o primeiro dia. Aos meus amigos Trindade e Galrinho pelos largos anos de amizade e aventura. Aos meus amigos Constança, Bernardo e André pela ajuda ao longo do curso e pelo seu apoio. Um obrigado carinhoso à minha namorada Rita pelo carinho e felicidade que me oferece todos os dias.

À companhia de teatro da Adversidade pela criatividade e alegria que inspiram em mim.

E a todos aqueles que de alguma forma participaram na minha vida.

Sem vós não valeria a pena realizar este trabalho

Abstract

Copper based composites are used for several thermo-electric applications. However, low strength, contaminant sensitivity and low service temperatures limit both applications and production methods. The development of a manufacturing method capable of providing a stronger copper matrix, with higher thermal stability, while minimizing transport property loss is imperative.

Graphite and alumina particles have been used to produce copper composites with improved dispersion strengthening and thermal stability. To increase matrix strength and copper recrystallization temperature silver was also added: the combined effect of these properties fosters milling efficiency.

This work approaches the production of 2wt% alumina, 2wt% graphite reinforced copper matrix composites, with or without 1.6wt% silver addictions, via high energy milling. The synergistic use of copper for milling media constitutes a paradigm shift in contrast to previously used media that emphasised high hardness as the optimal choice.

5 gram powder batches were milled up to 8 hours, at 200 RPM, in argon. A minimum copper crystallite size, as determined by XRD, of 21nm, 18nm and 20nm were respectively obtained for the Copper-Graphite, Copper-Graphite-Alumina and Copper-Graphite-Alumina-Silver systems. The maximum obtained ultra-microhardness values, HV0.025, were respectively 199±18, 220±27 and 221±8. Silver addition increased powder mass yield from 21% to 56% for 8 hours milling, providing an answer to losses by powder welding to the milling media.

Keywords: Copper; Nanocomposite; Mechanical Alloying; Alumina; Graphite; Silver

.

Resumo

Os compósitos com matriz de cobre são usados em diversas aplicações termo-eléctricas. No entanto, a baixa resistência mecânica, a sensibilidade a impurezas e as baixas temperaturas de serviço limitam simultaneamente as suas aplicações e os processos de fabrico. O desenvolvimento de um método capaz de produzir matrizes de cobre mais resistentes, com maior estabilidade térmica e sem a perda de propriedades de transporte é fundamental.

A grafite e a alumina tem sido usadas para aumentar a resistência mecânica e estabilidade térmica do cobre. A prata aumenta a resistência mecânica e a temperatura de recristalização do cobre potenciando o aumento da eficiência de moagem.

Neste trabalho produziu-se, por moagem de alta energia, compósitos com 2% em peso de alumina e grafite, com ou sem adições de 1.6% em peso de prata. A escolha de meios de moagem de cobre, sinérgicos, constitui uma mudança de paradigma, contrastando com os meios tradicionais de elevada dureza.

As moagens de 5 gramas de pó foram realizadas até 8 horas a 200 RPM em Árgon. O tamanho de cristalite mínimo obtido foi 21nm, 18nm e 20nm, respectivamente para os sistemas Cobre-Grafite, Cobre-Grafite-Alumina e Cobre-Grafite-Alumina-Prata. As ultra micro-Durezas, HV0.025, máximas obtidas foram, respectivamente, 199±18, 220±27 e 221±8. Para moagem de 8 horas, a adição de prata provocou um aumento do rendimento mássico de 21% para 56%, fornecendo uma solução para as perdas de massa devidas à soldadura ao meio de moagem.

Palavras Chave: Cobre; Nanocompósitos; Mecano-Síntese; Alumina; Grafite; Prata.

Index

List of Figures

List of Tables

List of Acronyms

BPR- Ball to Powder Ratio
BSE- Backscattered Electrons
DSI – Deep Sensing Indentation
EDS – Energy Dispersive Spectroscopy
ETPC - Electrolytic Tough-pitch Copper
FWHM – Full Width at Half Maximum
GND – Geometrically Necessary Dislocations
HV – Hardness Vickers
IACS – International Annealed Copper Standard (Conductivity)
ISE – Indentation Size Effect
IST – Instituto Superior Técnico
MO – Metal Oxide
MA – Mechanical Alloying
MMC – Metallic Matrix Composites
OPS – Oxide Polishing Solution
RPM – Revolutions per Minute
SE – Secondary Electrons
SEM – Scanning Electron Spectroscopy
SPS – Spark Plasma Sintering
XDR – X–Ray Diffraction

List of Symbols

Ag – Silver
Cu – Copper
Cg – Carbon with Graphite structure
D – Crystallite mean size
D peak – Graphite peak in raman spectroscopy around 1300 cm^{-1}
D_x – Diameter over X% of the powder sample
g – gram
G peak – Graphite peak in raman spectroscopy around 1580 cm^{-1}
Cg – Carbon with Graphite structure
h – Hour
J - Joule
k – kilo (10^3)
m – meter
M – mega (10^6)
min – minute
mm – millimetre

nm - nanometre

N – Newton

Pa – Pascal

R -- Ideal Gas Constant

REF – Reference

s - second

T – Temperature (Kelvin)

wt% - Weight Percentage

ΔQ – Activation Energy

θ – Angle of incidence

Λ – Wavelength

Chapter 1. Introduction

Copper engineering applications, from household computer heat sinks to first wall panel heat sinks in nuclear fusion devices, rely on its mechanical, corrosion and thermal and electrical transport properties [1]. However high temperature performance is always a concern due to grain growth and recovery [2] with copper displaying a recrystallization temperature as low as 360K [3]. This effect severely impacts applications of copper heat sinks and contactors, by requiring a reduction of service temperatures, and is incompatible with the high operation temperatures required for fusion reactors application [4] and resistance spot welding [5].

As an example, in resistance spot welding high temperatures cause softening of the electrode tips enhancing wear and leading to a deformation phenomenon known as mushrooming. This leads to an increase in electrode area with the number of welding cycles as show in Figure 1.

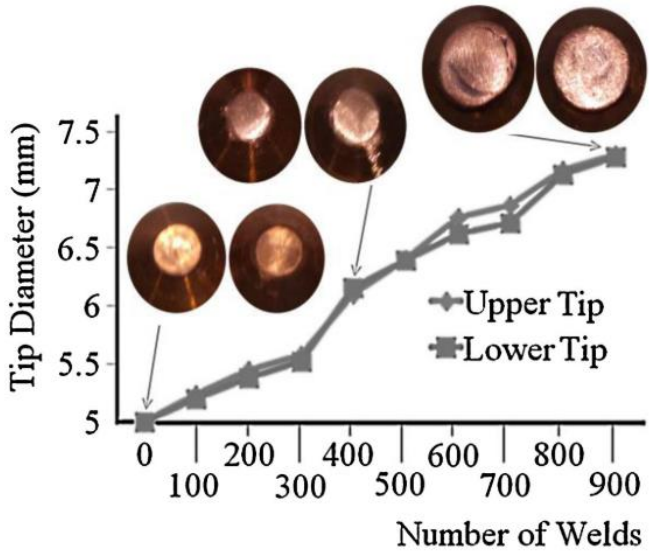

Figure 1 – Mushrooming effect; the of increase electrode tip diameter due to electrode wear during a welding cycle [6].

Copper matrix composites can be used to improve the surface properties of high conductivity copper and composite service temperatures, increasing simultaneously electrode lifetime and heat sink service temperatures.

This thesis aims at producing Copper based Metallic Matrix Composites, MMC, with different compositions, and characterize said composites, the objectives are:

- Production of MMC copper composites with graphite and alumina reinforcing phases and combinations thereof, as well as silver alloying.

- Production of hard and temperature resistant composites with low penalty for its transport properties. The target properties are a conductivity over 75% IACS, room temperature hardness over 300HV and improved wear and friction coefficient.

- Employing of the synergic milling approach to reduce contamination during the milling process and tackling of inherent challenges of this method.

This thesis consists of 6 chapters. The current Chapter 1 - Introduction, where the motivation, context and objectives of current work are laid out. Chapter 2 - State of the art., covers the current knowledge of the composites and alloying systems including an overview of the change in properties obtained in each system, the current knowledge on effect of the milling media in the incorporation of impurities is a also covered as a means to illustrate the necessity of a paradigm shift to employment of synergic milling. Chapter 3 - Experimental Techniques and Procedure, covers in detail the used materials, carried out experiments, and the material characterization methods, as well as some considerations on their working principles. 0 -

Results and Discussion goes over the challenges and obtained results for each system and characterization method. A critical discussion of each result is provided as well as considerations about each system benefits and compromises. Chapter 5 - Conclusions and Future Work, features the final conclusions and lessons from this work and offers follow up research to a better comprehension of the developed composite system and synergic milling approach. Chapter 6 - Bibliography, contains the list of sources used on this thesis.

Chapter 2. State of the art.

This chapter contains the current relevant knowledge to understand the context of this work, it also presents a review of the main topics discussed in this thesis. Section 2.1 covers the definition of composite materials and metallic matrix composites. The following subsections, 2.1.1 to 2.1.4, review the Graphite and Alumina systems in Copper composites as well as the addition of Silver as an alloying element to Copper composites. Section 2.2 presents an overview of the working principles of Mechanical Milling covering, on subsection 2.2.1, the changes in powder morphology and crystallography, followed by subsection 2.2.2 providing an explanation of how powder contamination occurs under these experiments and how it can be avoided. Section 2.3 explores the risk of oxidation of stored copper powders and Section 2.4 describes how oxidized Copper powders can be reduced to their metallic state during milling runs. Section 2.5 reviews the most common consolidation techniques to form bulk composites using the milled powders.

2.1. Copper Composites

A Composite is a material formed by different materials separated by a clear interface. Composite design opens the possibility to attain new properties or enhancing already existing ones. Composite materials allow new functionalities and applications. Examples such as reinforcing a soft material with hard particles to raise wear resistance [7], or generating a synergic effect independent of material properties such as reinforcement of glass sheets with a polymer film to create shatterproof glass [8] prove that composites are a viable strategy to overcome the constraints of single materials. All interactions over the discontinuity between two materials are mediated through the interface [9]. As a corollary, an important caveat is that two distinct materials only behave as a composite if they are bounded by an interface, which is responsible for the interaction between matrix and reinforcement. These interactions range from load sharing to transport phenomena like thermal conductivity.

Copper composites are metallic-matrix Composites, MMC. MMC typically have higher strength to weight ratios, dimensional stability, temperature resistance and fatigue resistance when compared to unreinforced metals [9].

Copper MMC's typically have a high conductivity, provided by the copper matrix. Reinforcing particles are used to increase hardness and high temperature performance, featuring low solubility and diffusion in the matrix and with a similar thermal expansion coefficient. As such MMC are often reinforced with hard and temperature resistant ceramic particles [10,11], such as Alumina or Silicon carbide, in order to improve hardness, elastic modulus, creep and high temperature behaviour.

A range of composite systems are used to improve different properties according to the material requisites. In the present work Copper-Graphite and Copper-Graphite-Alumina composite systems are studied.

2.1.1.Copper-Alumina System

Copper alumina composites are the most common oxide dispersed reinforced copper matrix composites [12,13]. Alumina particles act as physical reinforcement by providing high strength and hardness. The addition of ceramic particles enables two different reinforcing mechanisms: the dispersion of oxide particles inside de matrix provides an obstacle to dislocation motion, according to the Orowan reinforcement mechanism; simultaneously oxide particles will pin grain boundaries preventing grain growth during consolidation and during high temperature work, increasing material strength accordingly to the Hall-Petch mechanism. Alumina works as a suitable ceramic reinforcement for the above mechanisms due to its high hardness as well as chemical stability in copper [10].

The addition of alumina will decrease electrical conductivity, with the amount of alumina and respective particle size and dispersion being the most important factors. Optimization of Copper alumina composites will require a compromise between mechanical properties and electrical conductivity [14]. The trade-off between hardness and electrical conductivity is outlined in Figure 2.

As a reinforcement alumina provides a double benefit: at low temperatures the addition of alumina will act as a physical reinforcement increasing hardness; at high temperatures alumina will prevent the degradation of the nanocrystalline material structure. When working as a composite alumina particles will share load with the copper matrix lowering the wear rate of the matrix [15].

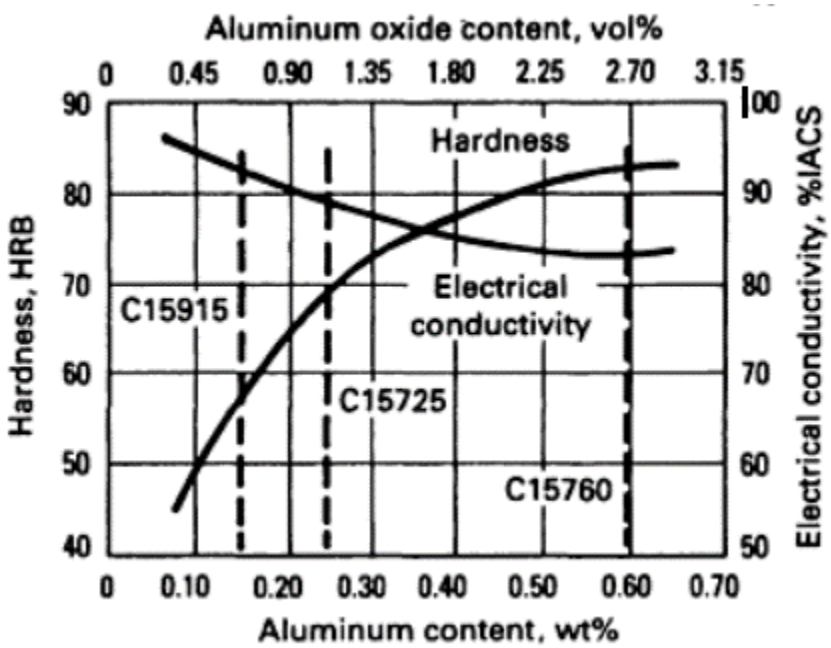

Figure 2 - Hardness and electrical conductivity of Copper composites as a function of Alumina content (adapted) [13].

The effect of oxide dispersion reinforcement does not only depend on the weight fraction of the reinforcing oxide. The Orowan reinforcement mechanism requires fine particles, below around 100nm in size [16], dispersed randomly in the copper matrix. A consideration when milling very fine particles is that these are not normally visible in SEM images, being only disclosed in TEM studies [17,18].

While reinforcement size, distribution and interface characteristics depend on processing parameters, and ultimately affect the composite properties, previous work on the copper alumina system outlines the trends of mechanical and transport properties dependence on the quantity of reinforcement addition. Table 1 resumes previous results for milled copper alumina composite systems.

Table 1 - Influence of oxide content in hardness and electrical conductivity of copper alumina composites. – Hardness units were converted using a soft metal conversion table [19].

Alumina weight %	Particle size (µm)	Powder Hardness (HV)	Hardness after heating (HV) (Heating Temperature (K): Sintering time (h))	Conductivity (IACS)	REF
0 (ETPC)		51	-	100	[20]
0.34	22.02	132	123 (1223: 1)	86.0	[14]
1	30.96	165	165 (1223: 1)	71.5	[14]
1.8	0.004	-	265 (1123: 2)		[21]
1.9	0.05	-	125 (1123: 2)	-	[22]
2.27	20	184	150 (1173: 1)	-	[23]
3	0.75	249	74 (1073: 5)	-	[17]
3.19	34.45	161	196 (1223: 1)	60.0	[14]
4	0.75	176	58 (1073: 5)	46	[24]
4.7	-	240	146 (1073: 5)	-	[18]
4.7	7	220	192 (1173: 1)	55	[25]
5.7	0.05	-	184 (1123: 2)	-	[22]
7.5	0.05	-	243 (1123: 2)	-	[22]
10.5	0.05	-	270 (1123: 2)	-	[22]

2.1.2.Copper-Graphite System:

Graphite has low thermal expansion coefficient, high corrosion resistance, good electrical conductivity, low solubility in copper and provides lubricating properties. Adding graphite to a composite opens the possibility to achieve a self-lubricating composite material. Besides graphite addiction avoids solid state bonding when pressure contacts develop at high temperature, minimising seizing risk and adhesive wear [26,27].

The main benefit of adding graphite to an MMC is the establishment of a graphite rich tribo-layer that allows the decrease of the wear coefficient, leading ultimately to the decrease of the wear rate. Additionally, the establishment of this tribo-layer does not come at the cost of transport properties of the composite into the work piece, due to the thinness of the formed tribo-layer, as well as the eventual discontinuities on the layer creating metal contacts spots [26].

The nature of the graphite lamellae is paramount to the success of self-lubricating contacts, and the ratio of basal plane area to lamellae edge surface area is considered an important feature in measuring the wear and lubricating behaviour of graphite. Finely subdivided small graphite crystallites provide a more effective contact wear behaviour, as edge surfaces are more chemically active binding readily with the atmospheric gas environment molecules [26,28].

The nature of copper-graphite interface is paramount in maintaining the mechanical and transport properties of the composite. Graphite usually establishes a poor interface with copper. This poor affinity might reduce the transport properties through it, reducing the overall properties of the composite. Metal coated graphite powders can be used to achieve a stronger binding: pre coating the graphite particles with a copper film by electroless plating [29,30] was successfully used to produce good interfaces. Copper coated graphite will bind easily to pure copper powders, reducing sintering times, and increasing density, conductivity and mechanical properties of the composite [31,32]. Coated graphite also decreases the wear rate in two different ways: firstly, it prevents graphite clustering, leading to a better spatial distribution as illustrated in Figure 3; secondly, it contributes to the formation of an adherent and compact tribolayer leading to a low removal rate during sliding tests [33]. Electroless coating was also performed with other metals such as silver producing similar results [34].

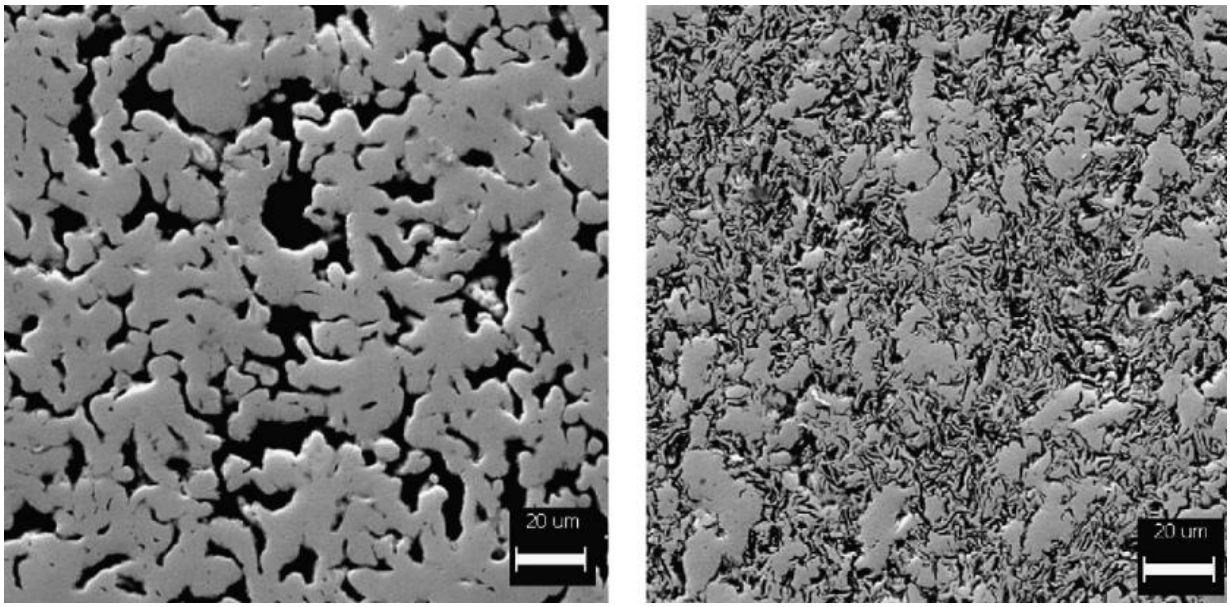

Figure 3- SEM Microstructure of Cu-graphite composites with 30% volume of graphite. Left, uncoated; Right coated [32].

Overall, the incorporation of graphite decreases the composite's yield strength and hardness [33], and slightly decreases thermal and electrical conductivity [31]. Additionally, the effect of graphite lubrication on the decrease of wear rate is limited to the incorporation of graphite debris into the tribolayer. At a critical concentration, not consensual but higher than 3wt% [32], the wear rate starts to become composition

independent. The tribological behaviour depends not only on the graphite quantity but also on its size, dispersion and applied load.

While reinforcement size, distribution and interface quality depend on processing parameters, and ultimately affect the composite properties, previous work on the copper graphite system outlines mechanical and transport properties dependence on the quantity of reinforcement addition. Table 2 resumes previous results for copper graphite composites. Systems using coated graphite were also included.

Table 2- Influence of graphite content and interface coating in hardness, electrical conductivity and tribological properties of copper graphite composites. Hardness units were converted using a soft metal conversion table [19].

Graphite Weight %	Friction Coefficient	Wear rate (mm3N-1m-1)	Hardness (HV)[1]	Conductivity (IACS)	Conditions (Load (N) / interface/ Sintering Temperature (ºC)/ Sintering Time (h) / method)	Ref
1.2	0.23	$6*10^{-4}$	94	79.8	12 / Coated / 750 /-/ Sintered	[35]
2.5	0.19	$5*10^{-4}$	90	72.4	12 / Coated / 750 /-/ Sintered	[35]
3.9	0.15	$4*10^{-4}$	81	70	12 / Coated / 750 /-/ Sintered	[35]
5.5	0.24	$6*10^{-4}$	56	38.7	12 / Coated / 750 /-/ Sintered	[35]
8	-	$1.9*10^{-3}$	794	-	200 / Coated / 900 /-/ Sintered	[33]
8	-	$2*10^{-3}$	785	-	150N/ Uncoated/900 /-/Sintered	[33]
9	0.15	$1.6*10^{-3}$	-	-	30N / Uncoated / 950 / 1.5 / HIP	[32]
9	0.13	$1.2*10^{-3}$	-	-	30N Coated / 950 / 1.5 / HIP	[32]
15	-	$1.3*10^{-3}$	775	-	250N Coated / 900 /-/ Sintered	[33]
15	-	$1.4*10^{-3}$	765	-	100N Uncoated/900 /-/ Sintered	[33]
19	0.15	$5.7*10^{-4}$	-	-	30 N Uncoated / 950 / 1.5 / HIP	[32]
19	0.18	$6.4*10^{-4}$	-	-	30N Coated / 950 / 1.5 / HIP	[32]
20	-	$0.9*10^{-3}$	755	-	300N Coated / 900 /-/ Sintered	[33]
20	-	$1.1*10^{-3}$	745	-	100N Uncoated/ 900 /-/ Sintered	[33]

2.1.3.Copper – Graphite – Alumina system

The simultaneous addition of alumina and graphite reinforcements provide copper metallic matrix composites with different properties. Graphite reinforcements provide the self-lubricating and anti-seizing ability. Fine alumina dispersions increase composite strength and thermal stability[10] of the copper microstructure. The use of both systems also enables the interaction between alumina and graphite. The addition of alumina to graphite copper MMC is expected to improve the incorporation and homogeneous distribution of the graphite phase in the copper powders [36].

While there is little previous work carried out in the Copper-Graphite-Alumina system, Copper-Alumina-Carbon [37] research, featured on Table 3, provides a scope of each reinforcement role in the composite behaviour. It The alumina reinforcement increases the friction coefficient, however the stronger matrix allows a reduced wear rate. The addition of carbon nanotubes, CNTs reduces the wear rate.

Directly leading to a reduced wear rate. The simultaneous alumina and carbon reinforcement features both reduced friction coefficient and the lowest wear rate of all systems, a resume of Pan et al. work [37].

Table 3 - Influence of each reinforcing system on the tribological properties of copper MMC's as reported by Pan et al. [37]*, results where obtained for 3N, 0.094m/s over 10 minutes.*

System	Friction Coefficient	Wear Rate ($mm^3N^{-1}m^{-1}$)
Copper	0.24	$11*10^{-5}$
Copper – 0.5Alumina	0.32	$8*10^{-5}$
Copper – 1.5CNTs	0.10	$7*10^{-5}$
Copper – 0.5Alumina – 1.5CNTs	0.16	$4*10^{-5}$

2.1.4.Copper – Silver alloying

Solid solution hardening [38] postulates that alloyed copper will have improved strength independent of solute, this effect is also dependent on the degree of deformation of metallic powders, which makes it a suitable hardening mechanism for mechanical alloying. The anneal hardening effect was found to increase the hardness of copper alloys with 4% atomic content of silver by 40HV in comparison to pure copper samples, for 60% plastic strains [39].

Silver provides the most promising candidate for alloying copper as is addition produces the smallest decrease of electrical conductivity amongst all other elements, as illustrated by Figure 4 [40]. Even 0.3wt% silver composition does not decrease copper conductivity below 99,5% IACS. The same trend is verified for thermal conduction with remains above 99,5% for alloys with a similar silver content [41].

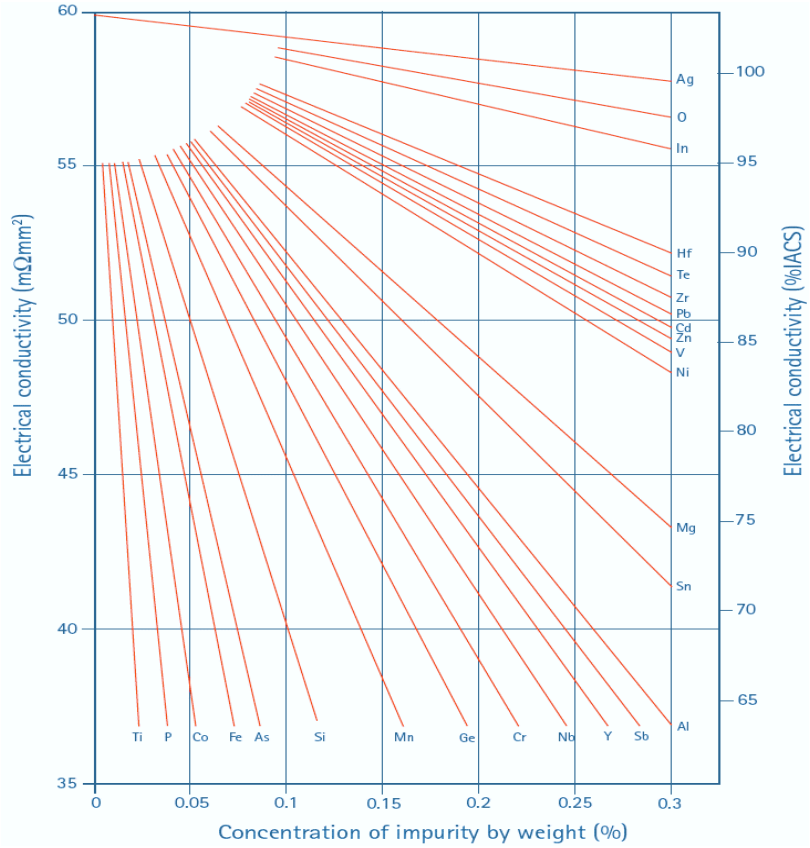

Figure 4- Decrease in copper conductivity according to impurity concentration [40]

It was reported [42] that mechanical alloying in the Cu-Ag system by ball milling~~,~~ is able to create a supersaturated face centred cubic structure in the entire range of compositions. Silver alloying increases copper recrystallisation temperature. Atomic additions of 4% silver raised the recrystallization temperature above 673K [39]. Most surprisingly, even small additions in the order of 0.05% elevated the temperature to about 613K [41,43]. Small additions of silver have been added to copper forming solid solutions to increase recrystallization temperature and tensile strength. A variety of patents for trolley wires [44,45] demonstrate that copper reinforcement by silver alloying can be successfully employed.

Silver is a promising alloying element for mechanical alloying by providing higher mechanical properties, especially the increase in hardness and recrystallisation temperature. These properties are relevant not only to material performance, but to the success of mechanical alloying by stopping recovery mechanisms during milling. This increases the fracture of cold worked copper powders, allowing the increasing rate of powder comminution. The cold fracture of welded copper on the surface of the milling environment also provides an increase in process efficiency. Silver is a suitable microalloying element, due to the increase in properties being available even at low alloying contents.

2.2. Mechanical Milling

Mechanical Milling, MA, is a powder processing technique that allows the production of powder materials by milling elemental powders. This technique requires the motion of milling balls against powder particles and colliding either against the vial wall or other balls. These repeated impacts provide a plethora of changes in the initial mixtures, such as physical changes in the powder particles which are described in the current section, or physically enabled chemical changes, described in the next subsections below.

Mechanical milling action consists of powders being repeatedly deformed, fractured and cold-welded. The energy source is provided by the transfer of the energy of collision between balls or between balls and the vial walls into trapped powder particles. The energy is mostly lost as heat, with only as little as 1% contributing to the deformation of powders [46].There are simple phenomena affecting the powders during mechanical milling: continuous deformation leading to work hardening, formation of flake-like powders leading eventually to fragmentation and powder size reduction; impacts between clean heated metallic surfaces causing the powder particles to cold weld, which contributes to an increase in powder size.

The described series of repeated random impacts, leading to ductile powder particle deformation and cold-welding, forms powder particles with a layered structure. The layered structure is refined throughout the process, leading to a reduction of layer thickness over time, as illustrated by Figure 5 and Figure 6.

Both powder size and crystallite size are refined through milling as well.

Work hardened powder particles will fracture leading to a decrease in particle size. However, powder particles are also subjected to recrystallization, enabled by the increase in temperature during milling which will offset the work hardening effect, and to cold welding leading to an increase in powder size.

The continuous deformation due to milling creates an high dislocation density, increasing strain. The arrangement of dislocations will form low angle boundaries within the grain, which rotate into high angle boundaries and eventually restart the process when these subgrains start piling up dislocations [47,48]. The refinement of crystallite size within a grain happens as cells form within cells, to minimize strain energy [49]. Contrary to these mechanisms that decrease grain size, there is a simultaneous and competing thermal activated process of recrystallization. It has been reported that a lower bound to crystallite size exists [47]. The theorical minimum grain size would be one that cannot sustain a dislocation pile up [50], However the experimental minimum, depends on the competition between dislocation pile up and the recovery mechanisms, and it was reported that it decreases with decreasing stacking fault energy and increasing melting temperature [47,48].

It should be observed that although crystallite size and powder size can reach a dynamic steady state, which is in both cases dependant on temperature enhanced recrystallization, the point at which each respective size becomes time independent isn’t the same. Crystallite size reduction and powder size variation happen simultaneously during milling but are independent from each other. As an example, for ductile systems with low work hardening powder size might increase due to cold-welding while crystallite size decreases, the described phenomena are observed in the current work.

For long milling times the cold-welding rate matches the comminution rate and a dynamic steady state in powder size is achieved. The crystallite size reaches a dynamic steady state as well. At this point the powder particles reach a saturation hardness due to the accumulation of strain and present a narrow size distribution. Milling after reaching, this so-called crystallite size, steady state in the mechanical milling process should be avoided because while neither powder size or crystallite size are being reduced milling is still taking place, wasting energy and risking powder contamination.

2.2.1.Mechanical Alloying of Metallic Powders

A powder batch containing multiple elemental powders, when mechanically alloyed, will mix the different powders, welding then and creating composite layered powders. Given a lengthy enough milling run the powder particles will feature the same proportion of elements as the initial powder batch.

Brittle additions, such as alumina, will behave differently than ductile additions. In the first stages of milling brittle particles get fragmented and trapped on the surface of the ductile particles. With the progression of the welding cycles, the reduction of the interlamellar spacing will provide a route for the dispersion of brittle particles enabling oxide dispersion strengthening.

If any component, either brittle of ductile, is soluble then the reduction of lamellar thickness, continuous welding, creation of new surfaces along fractured particles and temperature rise enables an increase the diffusion kinetics[51]. Simultaneously defect creation by continuous deformation extends the solid solubility of the system. Solubilization of different metal atoms lead to a change in the host lattice parameter, as atoms with different sizes start sharing the same crystalline structure. In the case of the current system it is claimed that silver is soluble in copper powders when mechanically milled [42].

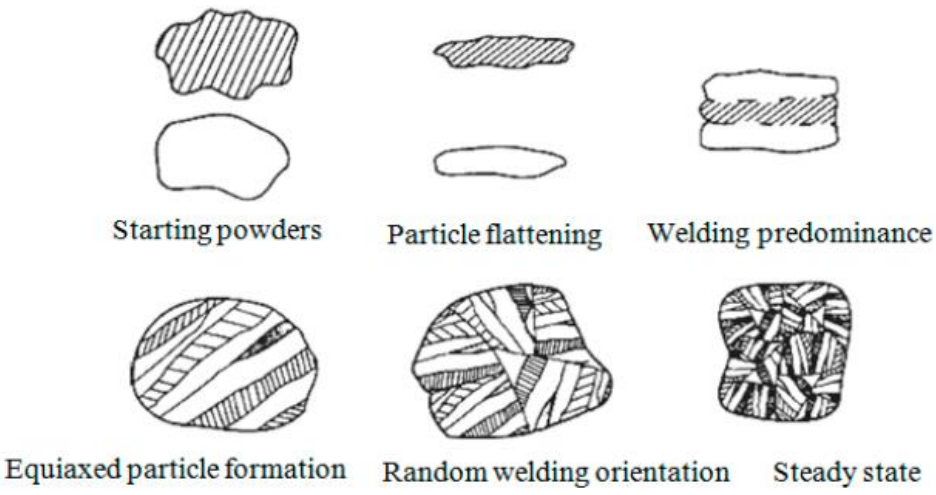

Figure 5 - Evolution of ductile powders during mechanical milling [51].

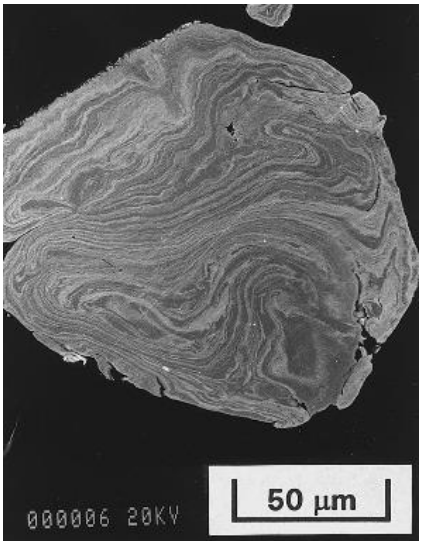

Figure 6 - SEM image of ductile layered particle obtained by milling Copper and Silver [46].

The milling process usually implies some interaction between milling media and powders beyond energy transfer trough impact. There is always some amount of mass transfer between the powder and the medium. This can lead to decrease in the batch mass due to powder welding to the medium, leading to a decrease in the process output and efficiency. The opposite can also happen, leading to an increase in the batch mass due to grinding medium debris joining the powders, acting as a source of powder contamination. Prevention of these processes will be further developed in subsection 2.2.2. However a trivial solution consists in avoiding milling after reaching the steady state in size reduction.

As a corollary mechanical milling is a process subjected to a diminishing returns law [52] where structure refinement is more intense for shorter milling times while the loss of efficiency (or incorporation of contaminants) is constant for all times.

2.2.2. Contamination and the influence of milling media

Contamination of milled powders is an inherent disadvantage of the mechanical milling technique, as the same mechanisms that make alloying possible will facilitate, (such as small powder size, availability of surface area and formation of new surfaces and layered powders), the incorporation of contaminations from the milling environment into the powder.

Impurities in the milled powders may come from different sources: impurities existing *a priori* in the initial batch of milling powders; products of reaction from the milled powders with the milling atmosphere, such as oxides; and milling media debris arising from balls and vial, being incorporated into the powder mixture.

The reduction of each contaminant source in the powder mixture is paramount. The use of high purity powders and protective milling atmospheres are straightforward solutions to the two first sources of

contamination. However, incorporation of milling media debris into the powders is very difficult to prevent, as the same attrition and collision forces responsible for the fracture of powder particles are acting on the vial walls and balls. For instance, when milling copper-graphite powder mixtures with alumina media [53], milling balls can lose up to 20% of their mass after 16 hour milling cycles. Taking into account that milling balls are usually used with a ball to powder, *BPR*, mass ratio of at least 10:1, this conservative approximation (no debris from the wall is accounted), implies that at the end of the milling process most powder comes from the milling balls. Similarly, milling with steel media also reported high contamination, with 20% atomic iron contamination after 24 hours of milling [54], with contamination reaching up to 40% in milling runs around hundreds of hours [55] . Incorporated powder is often abundant enough to contaminate X-ray diffractograms [56].

Some principles can be used to attenuate the incorporation of debris; the use media with higher hardness [57] than the powder can minimize the wear of the balls and vial walls. However, contamination cannot be completely prevented using hard materials, because impacts between the balls and the vial wall will always be present. Using harder materials to reduce the amount of wear is seldom a satisfying solution, because it restricts the range of available powders and the milling media often outweighs the milled powder in a high proportion, so even small amount of mass loss will lead to high contamination of the powder.

Media contamination decreases with consequent runs [58], due to the formation of a cold welded powder coating over the milling media. Thus, a sacrificial powder batch to cover the balls and vial walls can be used to prevent collisions between uncoated milling media surfaces, producing what is described as a seasoned vial [47].

The most successful approach to minimize the contamination of milled powder requires a paradigm shift from reducing the amount of milling media wear to reduce the impact of contamination. The Synergistic Milling approach used in this work employs milling media of the same material as the powder mixture to eliminate the contamination of milling powders with foreign elements. Furthermore, a comprehensive study of milling media weight loss can enable the production of powder mixtures with tighter chemical compositions control by considering the synergistic powder content increase on the milled powder.

2.3. Oxidation of stored Copper Powders

At high temperatures the growth of copper oxide films is proportional to the temperature dependent diffusion flux. The growth of such oxides is generally modelled by a parabolic growth law. However, at ambient conditions contribution from diffusion is negligible to the celerity of oxide growth [59].

Pure copper oxidizes at ambient conditions in a 3 step process [60] involving: the formation of a native oxide Cu_2O layer, which is a P type semiconductor with O^{2-} anions on the surface and Cu^{+} cations on the metal/oxide interface. This setup generates an electrical field pulling Copper ions towards the surface with low chance of electron hole recombination. This electrical field is strong but decays with the oxide layer growth. The reaction between Cu^{+} and HO^{-} ions on the oxide surface [61,62] creates an overlayer of

metastable $Cu(OH)_2$ that will evolve into a CuO layer. Both oxides grow independently: the native oxide reaches values of 2.5 nm in the first hour, towards a stable thickness of 5.2 nm after 66 days; the CuO layer starts growing after one day and reaches a maximum stable thickness of 0.9 nm[61].

Stored copper oxides in laboratory conditions are expected to oxidize even when subjected to short exposure times, due to the very fast initial growth rate. The formation of thin oxide films (in the order of 10 nm) will affect the initial powder composition in proportion to the increasing copper powder surface area and the oxide thickness. Thus, even for powders stored in a purified argon glovebox environment, a small amount of oxygen is always present due to powder manufacture, handling and transport.

2.4. Mechanochemical Reduction of Copper

Milling can induce unpredicted chemical reactions, because reactions can be mechanically activated at temperatures lower than usually required [46]. The process of enabling or catalysing a chemical reaction through mechanical milling his often referred as Mechanochemical Milling, MC, or Reactive Milling.

Reactive milling provides enhanced kinetics for reactions in a twofold mechanism: by reducing powder size and exposing new reactive surfaces it decreases diffusion distances; and by increasing the diffusivity due to local temperature rise and to the generation of a high amount of defects leading to a lower activation energy for diffusion, ΔQ.

The classical [63] use of a metal with higher affinity towards oxygen for the reduction of powder metal oxides raises two challenges: the reduction of the reaction efficiency with time as reaction products limit the contact between reagent interfaces; the difficulty of separating the oxide products from the metal products due to their intimate mixing (reduced metal powder and formed metal oxide) due to the milling process. In the case of CuO, total reduction was successfully achieved using Ca, Fe, Mn and Al [22,63].

The production of gaseous species, allowing the uninterrupted formation of fresh metal oxide surfaces ready for reaction and delivering a direct separation of products, represents an alternative route to overcome most of the identified challenges.

Thus, a promising route to deliver metallic copper powders free of surface oxides involves the use of C (graphite) with the aim of producing CO_2 [64]. Most of the work reported on copper oxide mechanochemical reduction by carbon targets the full reduction of copper oxide powders, Cu_2O [65] or CuO [64,66], to metallic copper.

Equation 1 shows the overall low temperature reduction of cupric oxide by carbon:

$$CuO + C \rightarrow 2Cu + CO_2 \quad (1)$$

The reduction provides a negative free energy change in the order of 150 KJ/mol and evolves in a two-step reaction with the partial reduction of cupric oxide to cuprous oxide [64]:

$$CuO \rightarrow Cu_2O \rightarrow Cu \quad (2)$$

Previous work, featured in Table 4, may provide a general envelope for the used milling conditions:

Table 4- Mechanochemical Reduction Experiments featuring the most important variables and results

RPM	BPR	Ball Mass (g)	Carbon Molar (excess%)	Reduction Start (h)	Reduction End (h)	REF
-	12:1	8.2	40	9	24	[64]
-	20:1	20.3	0	30	150	[66]
-	20:1	20.3	50	30	100	[66]
300	12:1	-	40	No Reduction	-	[65]
300	35:1	-	40	30	100	[65]

Important aspects of copper oxide reduction by graphite to consider are the increase of gas pressure inside the vial, and the copper oxide/carbon molar ratio in the batch.

The build-up of carbon dioxide produced by copper reduction in a sealed vial will cause an increase in CO_2 pressure. The pressure observed in similar experiments may reach up to 13 Bar [64]. However the decrease in free energy change in negligible [67]. Studies on the influence of the carbon/oxygen molar ratio [66] showed that the use of the stoichiometric amount of carbon could not reduce copper effectively. The low availability of carbon allowed the reduction to cuprous oxide but not to copper. Mixtures with excess molar carbon/oxygen molar ratio (150% and 200%) hindered the formation of Cu_2O in the later stages of milling, by providing higher carbon availability and successfully produced reduced copper powders.

To the best of my knowledge no reports were published regarding the behaviour of copper powders with minor Oxygen contamination and superficial copper oxides. However, the reduction process should follow the described pathways, and no copper oxide should be present after milling with graphite.

2.5. Sintering of Copper nanostructured powder composites

Consolidation of milled powders is an important step in the production of composites. Two main objectives are targeted: to attain a bulk high apparent density; to avoid the occurrence of grain growth that would invalidate the previous strength increase enabled by the milling experiments. Increasing the apparent density of copper MMC is a necessary step to achieve higher hardness and wear resistance as well as higher thermal and electrical conductivity [14,31].

The high sintering temperatures may cause copper grain recrystallization and growth, leading to the loss of the nanocrystalline structure inside the bulk composite [68] while mechanically dispersed particles hinder grain growth [23,69].

Consolidation techniques must be designed to achieve a balance between the increase of apparent density and coarsening of the structure.

Different consolidation techniques are available to produce bulk copper samples from nanostructured powder composites: hot isostatic pressing (HIP) [70,71], the most common method for sintering MA powders; hot extrusion [68] ; and also Spark plasma Sintering (SPS) [72,73].

Hot extrusion [68] produces dense materials with minimal grain growth, additionally the nature of the process can introduce anisotropy to the bulk materials, SPS can be used to achieve consolidation while

minimizing grain growth due to the use of low temperatures over short periods of time, while featuring fast heating and cooling cycles [72,74].

Chapter 3. Experimental Techniques and Procedure

The current chapter provides a scope of the methodology employed with the objective of providing reproducibility and transparency to the developed work. Section 3.1. provides a description of the materials used and subsections 3.1.1 to 3.1.4 describe each of the elemental powders used and their respective chemical purity. Section 3.2 provides an explanation of the experimental milling process guaranteeing reproducibility of the current work in order to obtain the powder samples. Section 3.3 contains the information of the experimental characterization. Subsection 3.3.1 describes the sample mounting and cleaning processes used and considerations made in order to account for the handling during characterization and subsections 3.3.2 to 3.3.5 offer insight into the characterization techniques, such as X-ray diffraction, Scanning electron microscopy, Raman spectroscopy and Hardness testing used along with a fundamental description of their working principles.

3.1. Materials

This section provides a description of the starting materials, information is provided base on the supplier product information. Further characterization of the base materials by SEM, XRD and Raman Spectroscopy is presented under the respective section.

3.1.1. Copper

Electrolytic Copper was used as the base material. These powders feature a dendritic particle shape, Figure 7, and were supplied by Pometon. According to the supplier more than 98% of the powder weight features a particle size under 63 µm, chemical purity of copper is, at minimum, 99.7wt% with a contaminant oxygen value around 0.08wt%.

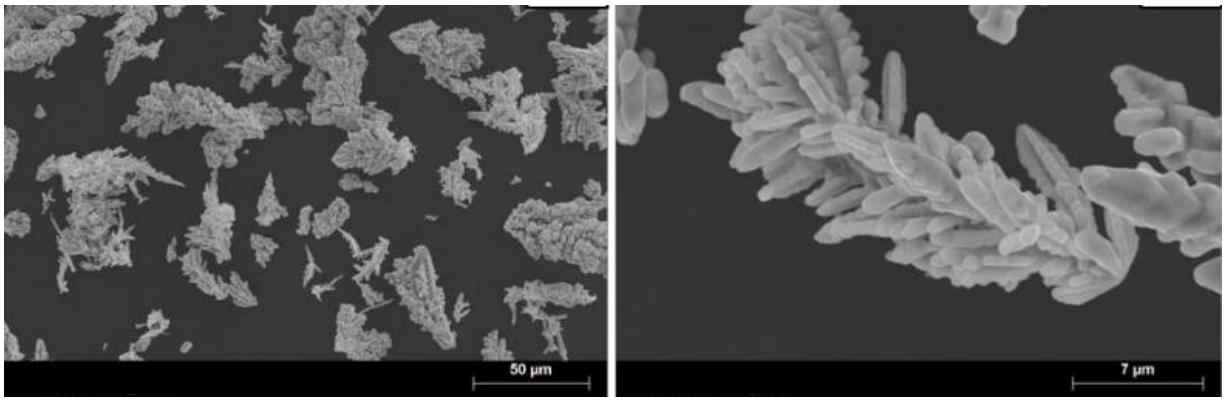

Figure 7- SEM image of the initial copper powder, this image was provided by a previous characterization of the same batch [75].

3.1.2.Graphite

Graphite was supplied by Imerys. Table 5 presents the supplier information for the synthetic TIMREX KS4 grade.

Table 5 – Particle size and typical contaminant information in the supplied graphite powders

Particle size (µm)	d_{10}	1.2
	d_{50}	2.4
	d_{90}	4.3
Contaminant typical value (ppm)	Fe	135
	Si	90
	Ca	90
	S	50
	Other elements	30

3.1.3.Alumina

Alumina was supplied by Almantis. Table 6 presents the supplier information of the reactive CT3000SG Alumina grade.

Table 6 - Particle size and contaminant value in the supplied alumina powders

Particle size (µm)	d_{50}	0.5
	d_{90}	2.0
Contaminant maximum value (%)	Na_2O	0.1
	Fe_2O_3	0.03
	SiO_2	0.07
	CaO	0.03
	MgO	0.1

3.1.4.Silver

Silver was supplied by Sigma–Aldrich. Table 7 presents the supplier information of the 327085 Silver grade.

Table 7 – Particle size and contaminant value in the supplied silver powders

Particle size (µm)	3.2	
Contaminant maximum value (ppm)	Sodium	12.5
	Iron	2.6
	Copper	0.5
	Magnesium	0.4
	Calcium	0.2

3.2. Mechanical alloying - Equipment and working principles

Milling was carried out on a Retsch PM100 planetary mill. Figure 8 illustrates its working principle. Planetary mills develop two different motions. The rotation of the sun disk, the disk supporting the grinding vial, and the vial rotation around its own axis in the opposite direction. In the case of the Retch PM100 the ration between the rotation speed of the sun plate and the rotation speed of the vial is 1:2. Milling speed always refers to the sun disk rotating speed and is expressed in rotations per minute (RPM). The sum of the centrifugal forces provides the necessary ball motion to grind the powders: friction from the balls running inside the vial, grounding the material, and collision resulting from the balls lifting off and flying through the vial and colliding on the opposite wall.

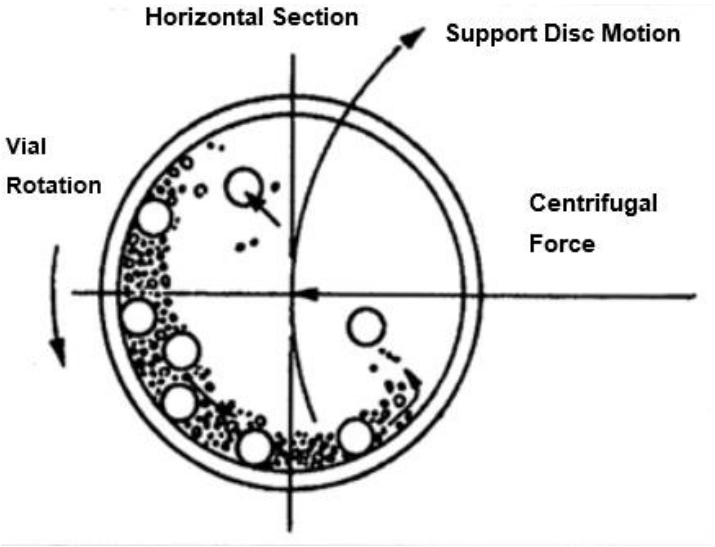

Figure 8- Diagram of nongravitational forces acting upon the balls inside the vial (adapted) [53].

Mechanical Milling is a complex process, with many variables interacting together. Attempting to discuss then individually can only provide an incomplete account of their effect due to their inherent interdependence. Researchers often resort to a more holistic approach and characterize the process in terms of impact energy and cumulative energy which is the total sum of impact energy delivered by the system during the time of milling [76].

Synergistic milling was employed to reduce the contamination of the powders with foreign debris from the media. So, the milling system consists of a Copper Vial, Copper balls, made from ETPC, and copper based powders with varying constituents which are specified in Table 8.

Table 8 - Copper based powders mixtures and respective weight composition

Powder mixture acronym	Copper (mg)	Carbon graphite (mg)	Alumina (mg)	Silver (mg)
Cu-Cg	4900	100	0	0
Cu-Cg-Al_2O_3	4800	100	100	0
Cu-Cg-Al_2O_3l-Ag	4800	100	100	80

The copper vial volume was 250 mL, and eleven copper balls with a radius of 5 mm and a mass of 4.7 grams were used to grind copper powders with varying compositions. Each milling run used 5 grams of powder mixture and 11 copper balls, providing a BPR of 10:1. Considering a compaction factor for randomly stacked spheres inside a vial of 0.65 [77] the vial filling ratio is under 5%, which is important to provide the balls a free trajectory of flight inside the vial in order to deliver the maximum impact energy against the opposite walls [78].

Milling runs for the Copper-Carbon composites were carried out with different milling rates. However, in all runs over 200 RPM the cold-welding rate lead to negligible mass yields, as demonstrated by Figure 13. To obtain yields compatible with the formation of bulk pieces the 200 RPM milling rate was selected for all further studies. Before starting the milling runs for a new composition, a sacrificial milling run was carried out for 8 hours, coating the milling media, to increase the yield of subsequent runs by forming a seasoned vial [46,47]. All milling experiments were performed starting with the longer runs. All milling cycles were carried out with stopping intervals to avoid overheating and to cool the mill media and milled batch. The tested milling program is described in Table 9.

Table 9 - Milling Programs for Different Milling Runs

Milling Run	Milling Program	Adopted acronym
8 Hours	30’ Milling + 30’ Stop X16	8h
1 Hour	30’ Milling + 30’ Stop X2	1h
30 Minutes	15’ Milling + 15’ Stop X2	30min
15 Minutes	15’ Milling	15min

In order to avoid powder oxidation, the vial was sealed with O-rings and filled inside a glovebox in a protective argon atmosphere. Post milled powders were always handled inside the glovebox and were exposed to an oxidizing atmosphere for instants before characterization.

When changing powder composition, the vial walls were machined to clean the copper surface and the balls were changed for new ones, as a means of maintaining the working principle of synergic milling.

Table 10 presents all milling runs performed and discussed in this work. An additional unmilled Copper sample – Copper Reference - was used in the characterization stages to provide a comparison point to the changes occurring during milling.

Table 10 - Powder compositions and milling conditions.

Powder composition	RPM	Powder mass (g)	BPR	Milling Times
Cu-Cg	200/400/600	5	10:1	1h; 2h; 5h
Cu-Cg	200	5	10:1	15min; 30min; 1h; 8h
Cu-Cg-Al_2O_3	200	5	10:1	15min; 30min; 1h; 8h
Cu-Cg- Al_2O_3-Ag	200	5	10:1	15min; 30min; 1h; 8h

3.3. Materials Characterization

This chapter aims to outline the experimental process and the respective working principles. Subchapter 3.3.1 describes the sample preparation method and practical considerations made due to the nature of the sample. Subchapters 3.3.2-3.3.5 provide a description of the characterization methods performed on the samples along with the most fundamental theorical considerations relevant to working with those methods.

3.3.1.Sample preparation

Besides direct characterization of as produced powders, powder cross sections were also prepared to characterize the entire powder volume.

Powders were hot mounted in Buelher KonductoMet powder, a carbon and mineral filled conductive resin. Hot mounting was performed in a Buehler Simplimet 2000 mounting press. The mounting cycle consists of a 7 minutes heating step at 160ºC followed by a 7 minutes cooling step. All mounted samples were grinded with SiC grinding papers and lubricated with water. Furthermore they were polished using diamond suspensions starting with 3 µm up to 1 µm, followed by an additional step using a custom made oxide polishing suspension obtained by enhancing OPS with 2% ammonia solution and 2% peroxide water solution, which are often used as an etching agent for copper, increasing the chemical activity of the polishing suspension.

Two problems were found during sample preparation:

Because powders were mostly very small around 100 µm they would get removed during grinding leaving the sample without any powder particles. In order to avoid powder removal during the grinding step, copper powders were premixed in a batch in order to form a powder rich resin layer which is indifferent to material removal as new surfaces still contain copper powders. Figure 9 provides a naïve illustration of how a resin rich layer will allow the sample to retain copper powders even after material removal via grinding.

Because copper powder particles are very soft complete scratch removal was difficult, additionally relying only on mechanical abrasion always carries some amount of deformation of the material surface. In order to obtain an improved surface finish, the above described custom oxide polishing suspension was produced. This chemical enabled physical polishing featured no surface scratches and was used in order to reduce the surface residual strain.

As OPS silica particles tend to adhere to the sample surface and additional cleaning step was performed involving ultrasound cleaning inside a water and soap solution, followed by ultrasound cleaning inside an alcohol solution.

All samples used in X-ray diffraction, Raman spectroscopy and hardness testing were prepared using the outlined method.

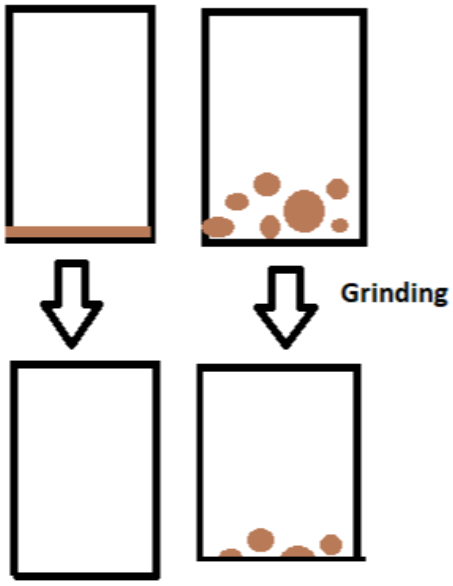

Figure 9- Susceptibility of samples to material removal via grinding. Powders mounted on the surface (left) Copper rich resin layer (right)

3.3.2.X-ray diffraction

R-ray diffraction was used to identify the presence of crystalline phases in the milled powders, as well as determining the effects of mechanical alloying and their extent on the reduction of crystallite size, residual strain, and lattice parameters. Pre-milled powder was also characterized to identify proper reference patterns.

The lattice parameter was calculated from Equation 3 which can be inferred from Bragg's law for cubic structures [79].

$$a = \frac{\sqrt{h^2 + k^2 + l^2}}{2sin\theta} \quad (3)$$

However, direct application of Bragg's law does not provide an accurate measure of the lattice parameter, as there are many sources of error. Among others, one comes from the uncertainty of the diffraction centre's position [80]. Diffraction originating from a region beneath the powder surface, with a vertical *h* shift, causes a shift in the apparent diffraction angle in inverse proportion to the diffraction angle and the goniometer radius R; as per Equation 4 and showed by Figure 10.

The Nelson Riley extrapolation [81,82] suggests that the intercept for θ = 90º provides a more accurate lattice parameter, eliminating the errors of specimen shift and X-ray penetration depth.

$$\Delta\theta = \frac{h\cos\theta}{R} \tag{4}$$

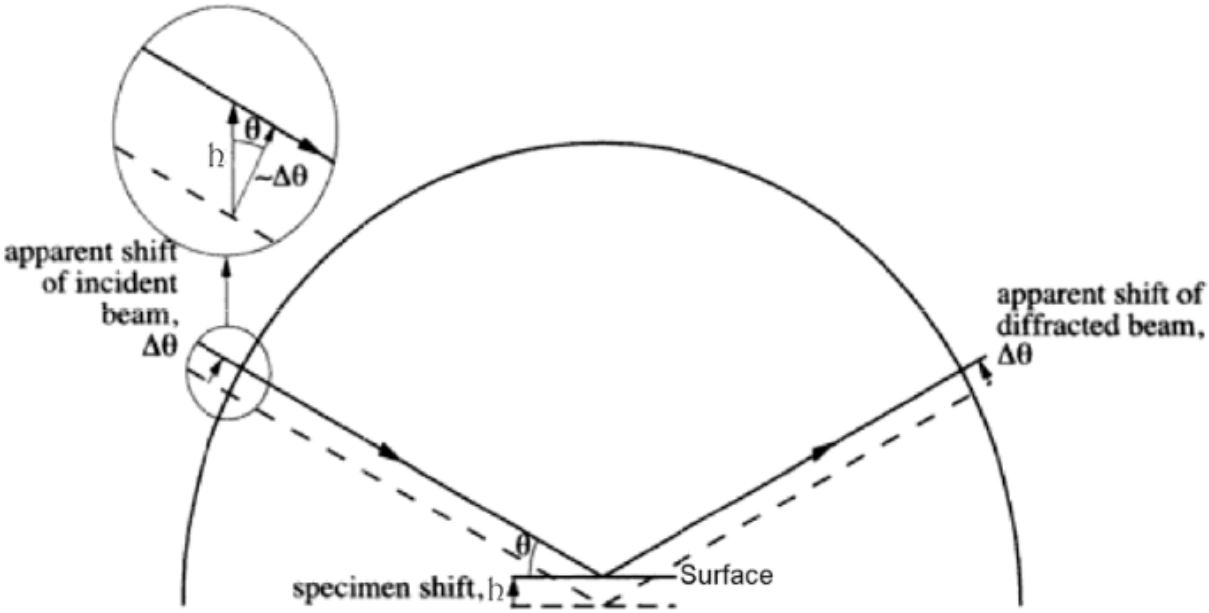

Figure 10 – Effect of sample shift, ħ, shifting the diffracted beam angle [79].

Crystallite size was calculated by Scherrer's equation (Equation 5) which relates peak broadening β to decreasing crystallite size D. Scherrer's equation does not consider the peak broadening effect of residual strain ε, providing only a lower limit to crystallite size. Williamson-Hall [83] equation considers and distinguishes both effects: β_c, the contribution of crystallite size to peak broadening and $\beta_{S,}$ the contribution of microstrain to peak broadening determined by Equation 7. Equation 6 can now be rewritten as Equation 88888. Plotting $\beta\cos\theta$ as a function of $2\sin\theta$ yields a linear equation from which *Y*, the intercept, is the contribution from the crystallite size and the slope is the strain contribution to peak broadening.

$$D = \frac{\lambda k}{\beta\cos\theta} \tag{5}$$

$$\beta = \beta_C + \beta_S \tag{6}$$

$$\beta_s = \frac{2\varepsilon\sin\theta}{\cos\theta} \tag{7}$$

$$\beta cos\theta = \frac{\lambda k}{\beta} + 2\varepsilon \sin\theta \quad (8)$$

Only copper peaks where analysed in X-ray diffraction. To minimise error the most intense peaks, which coincidentally are the lower angle peaks, were used to calculate the crystallite size and the highest angle peaks were used for lattice parameter size determination. Analysed copper peaks, their respective coordinate and use are detailed in Table 11.

Table 11- Mapping of copper plane peaks and respective use in X-ray diffraction analysis

Plane	Copper peak at 2θ(º)	Use
[111]	43.3	Crystallite Size
[200]	50.4	Crystallite Size
[220]	74.1	Crystallite Size
[311]	89.9	Crystallite Size
[222]	95.1	Crystallite Size
[400]	116.9	Not used
[331]	136.5	Lattice Parameter
[420]	144.7	Lattice Parameter

Diffractograms were obtained using an Bruker D8 ADVANCE Powder Diffractometer, with an acquisition time of 0.5 seconds and step size of 2θ=0.5º were used. Scans were carried out from 2θ=20º to 2θ=100º for all samples. Additionally scans, more time consuming but more accurate measurements, were carried out over smaller intervals when suited: 1) From 2θ=25º to 2θ=27º corresponding to the most intense graphite peak; 2) From 2θ=34º to 2θ=36º corresponding to the most intense alumina peak; 3) From 2θ=37º to 2θ=39º corresponding to the most intense silver peak; 4) From 2θ=133º to 2θ=148º corresponding to the highest angle peaks of copper.

Diffractograms were analysed using the X'pert Highscore software. Peak shape in the diffractogram was fitted using Pseudo-Voigt functions (or Pearson VII when necessary to obtain a better goodness of fit), considering Gaussian and Lorentz equations [84–86] as well distinguishing *K-α* and *K-β* originated peaks.

3.3.3.Scanning Electron microscopy

Scanning electron microscopy (SEM) uses an electron beam of accelerated electrons focused on a small (around 1nm-5nm) focal point impinging the sample surface. The surface backscatters or emits electrons, and X-rays that are collected on a detector providing information on the sample topography, crystalline structure and elemental. The scanning motion of the electron bean over the sample provides

information over a select surface area. SEM is a suitable method to observe details from the micrometre to the sub-micrometre range [87].

An a JEOL FEG-SEM model JSM-7001F equipped with an Oxford Light Elements EDS Detector was used in this work.

3.3.4.Raman spectroscopy

Raman spectroscopy is a class of optical reflection techniques with high spectral resolution used in the chemical identification and characterisation of molecules [88]. All these techniques are based on the Raman effect, occurring when polarized monochromatic light is inelastically scattered by a molecule.

Vibrational Raman spectroscopy, based on Raman scattering (where the molecules shift vibrational state), is the most widely used Raman technique [88]. A vibrational Raman spectrum contains the unique and highly resolved vibrational signature of the scattering molecule, that can be used as fingerprints for the characterization of molecules in solids, powders and solutions [88]. The spectrally filtered incident radiation interacts with the material, inducing a dipole moment within a given molecule based on its polarizability, followed by photon emission. In inelastic scattering the energy of the emitted photon is of either lower (Stokes shift) or higher (anti-Stokes shift) frequency than the incident photon, resulting that after the scattering event the sample is in a different vibrational state. Stokes and anti-Stokes shifts always feature the same shifts in either the positive or negative direction as illustrated in Figure 11. The molecules may either shift rotational, vibrational, or electronic state during the scattering, depending on the molecule and the specific experimental conditions. Inelastic scattered photons are shifted in frequencies proportional to the energy between the vibrational energy levels in the molecule, allowing to identify the corresponding functional groups, while the intensity of the Raman scattering is proportional to this polarizability change [88].

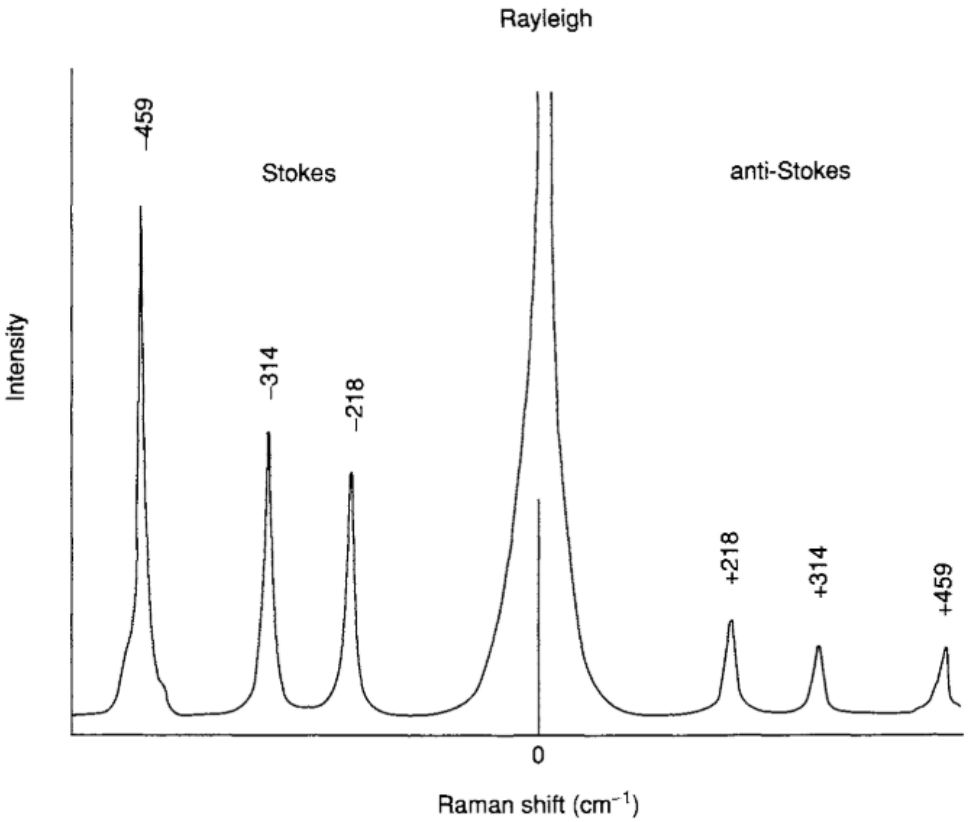

Figure 11 – Raman spectrum shift of CCl4, [89] *featuring Stokes and antiStokes shifts.*

In the current work, Raman spectroscopy was used to identify and characterize changes in the graphite phase as a function of milling time. The shape, position and intensity of characteristic Raman carbon peaks, in as-supplied graphite and in milled samples containing 2wt% graphite, were used to semi-quantify the evolution of the amorphous graphite fraction and to evaluate the extent and type of defects present. The most prominent features in the Raman spectrum of graphite are the *D* and *G* peaks, respectively around 1300 cm^{-1} and 1580 cm^{-1} [90]. The *D* peak is activated when border defects are present in the carbon crystalline lattice and is thus related to graphite crystallite size. The *G* peak reflects the degree of symmetry of the crystalline lattice and relates with the distance between point defects in the carbon network [90,91].

Many relationships can be inferred from the Raman spectra specifically:

$$Peak\ intensity\ ratio = \frac{I_D}{I_G} \tag{9}$$

Where I_D and I_G are the intensity of *D* and *G* peaks respectively.

$$Peak\ area\ ratio = \frac{A_D}{A_G} \tag{10}$$

Where A_D and A_G are the areas of *D* and *G* peaks respectively.

$$G\ peak\ broadening = \mathrm{FWHM}\ (G) \tag{11}$$

G peak broadening is characterized by the full width at half maximum, FWHM, of the *G* peak.

Peak intensity ratio, I_D/I_G, is inversely proportional to mean crystallite size [90,91] and characterizes the amount of edge defects (size related defects) [92], while peak area ratio, A_D/A_G, represents combined information on size defects and point defects (i.e., total defects) [92]. Additionally, the decrease of A_D/A_G combined with *G* peak broadening (characterized by the FWHM increase) has been related to the initial stages of graphite amorphization [90,93,94].

Raman scattering not only depends on the species, but also on specific experimental conditions [88]. In particular, while *G* peak broadening has been reported to be independent of sample polishing [95], *D* peaks intensity decreases unpredictability when subjected to polishing, which leads to overestimation of crystallite size. Therefore, *G* peak broadening is a parameter independent from the changes that affect the *D* peak intensity when polished and is considered a more precise parameter when characterizing the decrease in crystallite size [95].

In this work all previous parameters are reported as all of them follow the evolution of the amorphous graphite contentment during the milling process and were found to change accordingly and pointing to the same conclusion, allowing redundancy in observed changes.

Analysing the graphite content inside the composite powders poses some challenges; the low amount of graphite content coupled with the lack of homogeneity in the composite powders (most evident in the 15 and 30 minute runs), with some powders showing no graphite made the observation of high intensity Raman spectrums difficult. A spectrum was considered valid when the intensity of either *G* or *D* peaks were noticeable. However because graphite particle dispersion inside copper powder dispersion lacks homogeneity, there is no method available of preventing confirmation bias, because the employed definition of a valid observation excludes some of the samples a priori, such as samples with low graphite content, thus low intensity, in favour of clearer Raman spectra.

3.3.5.Mechanical testing

Hardness is a local measurement of material resistance to plastic deformation under penetration. There exists a plethora of indenters and indentation techniques, however all methods describe hardness as the local material resistance to plastic flow caused by indenter penetration. Hardness is not a fundamental material property, but it can be used to outline other material properties such as the yield stress.

When testing small specimens such as milled powders, indentation load becomes an important factor. High loads lead to deeper, wider indentations. The resulting indentation is therefore influenced by the mounting resin properties under the powder particle, decreasing the accuracy of the measurements. In order to achieve reliable measurements nanoindentations, featuring submicron indentation depths, were performed using a depth sensing indentation (DSI) method [96].

Powders feature an intrinsic heterogeneity due to the stochastic ball impacts during the milling process. This implies that even reliable measurements will feature some dispersion of values, which is expected to be more pronounced for short milling times.

Studies on nanoindentation [97] indicate that very small indentations are subjected to an indentation size effect, *ISE*, [98]. Measured hardness increases with the square root of decreasing indentation size. The deformation of a material under an indent generates geometrically necessary dislocations, GND, to account for the shape change in the indented volume. Figure 12 highlights these dislocations, which are contained inside a plastically deformed volume arranged in circular loops. Indentation under a critical volume lead to higher dislocation densities, which increase the measured hardness for depths under a critical value which is material dependent. For monocrystalline copper (111), hardness becomes depth dependent for indentations depths under h_o =1.6μm [98,99].

The model first proposed by Nix-Gao [98] establishes a relationship between Hardness measurements at different indentation depths, and provides the formal template for the power law relationship between Hardness increase with depth decrease:

$$\frac{H}{H_o} = \sqrt{1 + \frac{h_o}{h}} \tag{12}$$

Many alterations have been suggested to the Nix-Gao model in order to obtain better fitting of experimental data, however they usually require the fitting of more parameters and such data analysis would be beyond the scope of the present work [100,101].

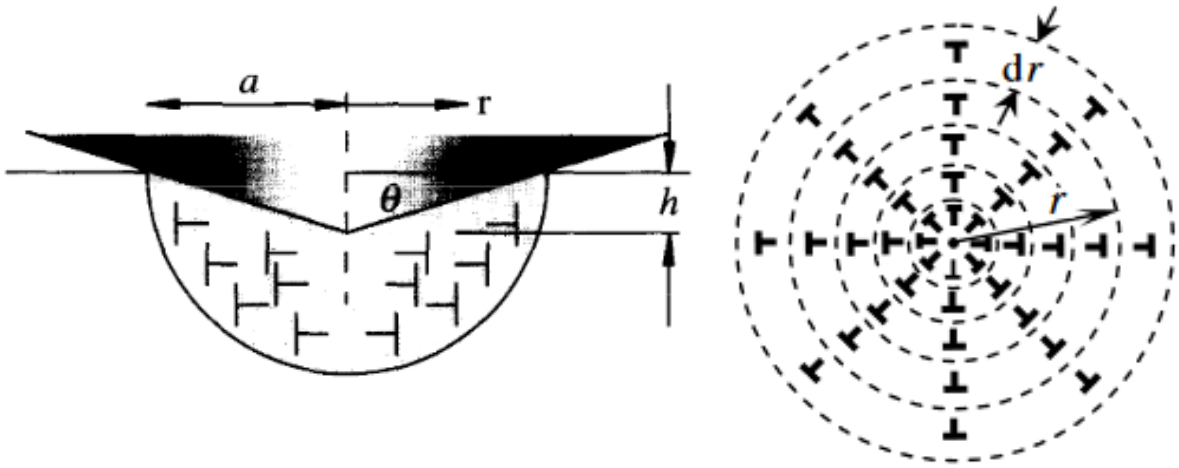

Figure 12 – Left – Geometrically Necessary Dislocations formed in a volume under the indentation [98]. *Right Top view of the circular dislocation loops* [100].

ISE have been widely studied for single crystals and polycrystals. Polycrystalline materials present a similar behaviour under nanoindentation, because, even in cold worked materials, indentation volume is contained inside a single grain [102].

Studies on ultrafine-grained, *UFG*, materials [99,103] and simulations [104] on small grain size samples report that nanohardness becomes size independent, as the indented volume starts to bridge over multiple grains. Accordingly, ISE is dependent not only on the indenter and indentation depth, but also on the crystalline structure, once penetration depth and grain size reach similar sizes

Nanoindentation tests were performed using a Shimadzu DUH-211S dynamic ultra-microhardness tester using a maximum load of 25 mN. The load increases at 4.4413mN/s up to the maximum load and is held for 15 seconds. Loading and unloading curves are analysed using the method described in [105]. Indentation tests were performed until a minimum of 10 valid indentations were obtained or the sample ran out of powders suitable for an indentation. A valid indentation was considered an indentation performed inside a copper grain and whose load and unloading curves had a coherent shape, free of environmental noise. Samples were finely polished in order to reduce the effect of surface topography and strain hardening in the measured hardness.

Only the bulk annealed copper reference is subjected to ISE. All other composite powders feature a nanocrystalline structure and feature a hardness value independent from indentation depth.

Even when using deep sensing indentation there is a clear difficulty in obtaining hardness values. Often copper grains are not big enough to contain the deformation, thus they could not contain the deformation zone inside a single powder grain. The following load transfer into the polymer matrix decreases and contaminates the hardness value. While this difficulty can be overcome by indenting an high number of powder grains in order to obtain an high number of valid measurements the powder rich polymer layer described in section did not always yield any measurable copper powders, this was

observable in– the Copper – Graphite system milled for 15 minutes and for the Copper – Graphite - Alumina system milled for 30 minutes.

A valid hardness measurement was considered a measurement that yields a hardness over 80HV0.025 which was the measured value from a reference electrolytic copper standard sample, had the indentation fully contained inside the powder volume, and featured no ambient noise.

3.4. Powder Mass yield

Mass transfer between the powder batch and the milling media is a chief concern of mechanical milling. Usually fractured powders from either the vial walls or the grinding balls join the powder acting as a source of contamination [106]. Measuring ball mass loss provides a qualitative measurement of contamination in milled powders. In synergic milling, contaminations coming from the milling media are, by corollary, inexistent. However mass transfer is always happening in parallel with mechanical milling, and a quantification of mass transfer is still relevant to the current work to estimate process yield and powder composition change.

Powder yield is defined as the mass relation between the powder input and the powder output according to Equation 13:

$$\text{Powder Yield}(\%) = \frac{\text{Powder output (g)}}{\text{Powder input (g)}} x\ 100 \tag{13}$$

Powder input is known for all milling experiments. After milling powder is scrapped from the walls and weighted. Runs are considered successful if they yield more than 1g (20% mass yield) of powder after milling. One gram is the is the amount of powder considered necessary to carry out all the characterization tests in the next chapter.

Chapter 4. Results and Discussion

In this chapter results regarding the milling experiments are presented and discussed. Section 4.1. addresses mass transfer between the milling media and the powder batch for all milled systems, along with considerations on the nature of this phenomena and how to reduce it in future synergic milling experiments. Section 4.2. delves into the Raman Spectroscopy results and characterizes the possible amorphization of graphite during the milling experiments. Section 4.3. covers the results of X-ray diffraction, in order to evaluate and crystallite size and lattice parameters evolution along milling experiments. Section4.4. discusses the SEM images of milled powders, addressing powder microstructure and possible welding and fracture behaviour. Section 4.5. presents and discusses the hardness measurements in milled powders, discussing the effects of milling time and powder batch composition.

4.1. Mass variation during milling experiments

While synergic milling is oblivious to powder contamination, it still features dynamic mass transfer by either milled powder welding to the milling media, or wear milling media debris joining the milling batch. Because milling was performed in an oxygen free atmosphere in the presence of a reducing agent, graphite, the absence of surface oxide layers leads to excessive cold welding. Thus, high milling rates, equal or above 400 RPM, were impossible to use due to negligible mass yield. Figure 13 shows how milling experiments carried out in the Cu-Cg system, at 400 RPM and 600 RPM deliver very low mass yield, even for 2h experiments. As such, all milling experiments were carried out at 200 RPM to stay above the 20% yield threshold.

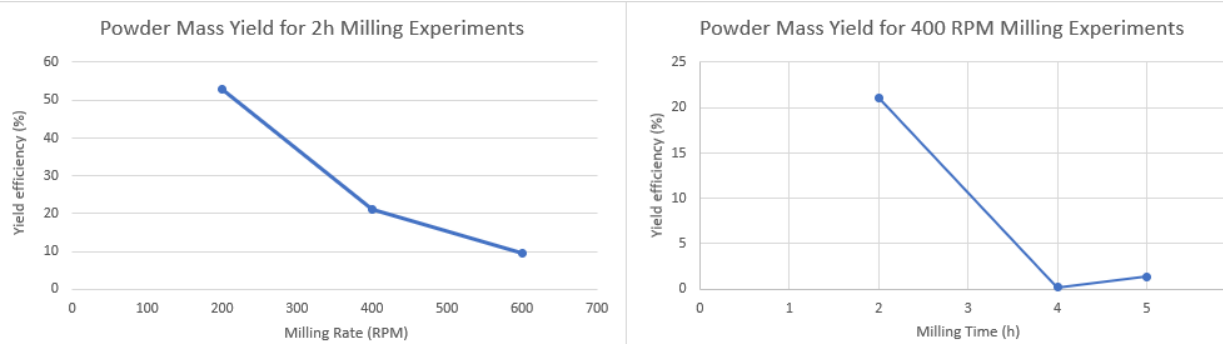

Figure 13 - Powder Mass Yield for different Milling Experiments in the Cu-C system. Left) For different milling rates; Right) for different effective milling time

However, even using a milling rate of 200 RPM, powder cold-welding to the milling media still occurs. Mass yield experiments are reported and discuss in this section. Result analysis should bear in mind that, for each system, a sacrificial 8h run was carried out before all experiments and that experiments were carried out starting from the longest run using the same milling jar and the same balls.

4.1.1. Copper – Graphite system

Figure 14 illustrates that powder mass loss due to welding into the milling media is ubiquitous and during milling a steady state between powder welding and powder fracture from the milling media is not achieved in the first 8+8 hours. Figure 14 clearly shows that the loss of process efficiency cannot be mainly attributed to ball mass variation and powder cold welding to the balls. The surface area of vial walls is close to seven times that of the balls. Therefore, most of the permanent mass exchange takes place between the vial wall and the batch loose powder or the powder coated balls. Thus, total experimental mass yield variation is attributed to the summation of balls mass variation (measured) and vial mass variation (deducted).

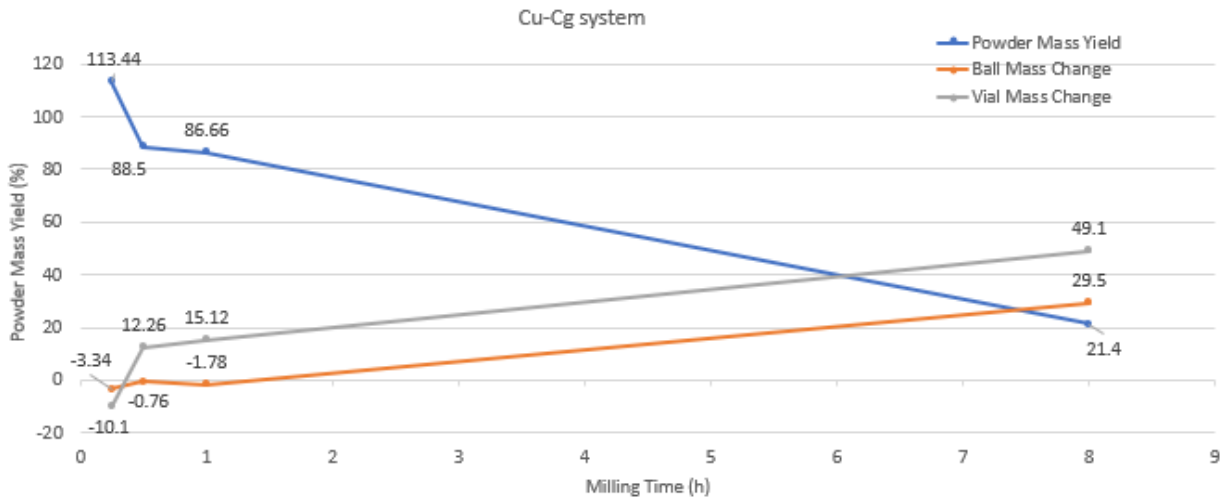

Figure 14- Powder Mass Yield changes for the Cu-Cg system.

The shortest runs with new powder (15 minutes) correspond to the longest cumulative run for the vial and balls. These runs feature a process efficiency over 100%. This is possible because these runs feature the highest amount of deformation hardened welded powders on the milling media surfaces, increasing the probability for these hardened surfaces to break of and join the powder batch increasing the process efficiency over 100%.

Following the same logic, because the 8 hours experiment was the first to be performed after the mandatory 8 hours running-in, it featured the least amount of hardened powders welded to the milling media surfaces, further skewing the mass flow exchange in favour of powder welding. This effect, created by the order in which the runs are performed, further accentuates the low mass wield in the longer 8 hour runs.

4.1.2. Copper – Graphite – Alumina System

As showed in Figure 15, the addition of alumina to the powder batch decreases the mass yield for all milling times, when compared to the Copper – Graphite system, while keeping the overall tendency.

Alumina reinforced copper composites are expected (and confirmed in section 4.5) to be harder and less ductile than Copper – Graphite composites. The addition of a hard component, alumina, and the milling of an overall harder and less ductile material should feature an increase on the milling media wear and the fracture of welded powders. Both would increase the mass yield and eventually accelerate the occurrence of a steady state mass flow between milling media and powder batch. In practice none of these effects were observed. While the ductility decrease due to the presence of alumina could have been overestimated, no motive was found to explain the decrease in process efficiency due to alumina addition.

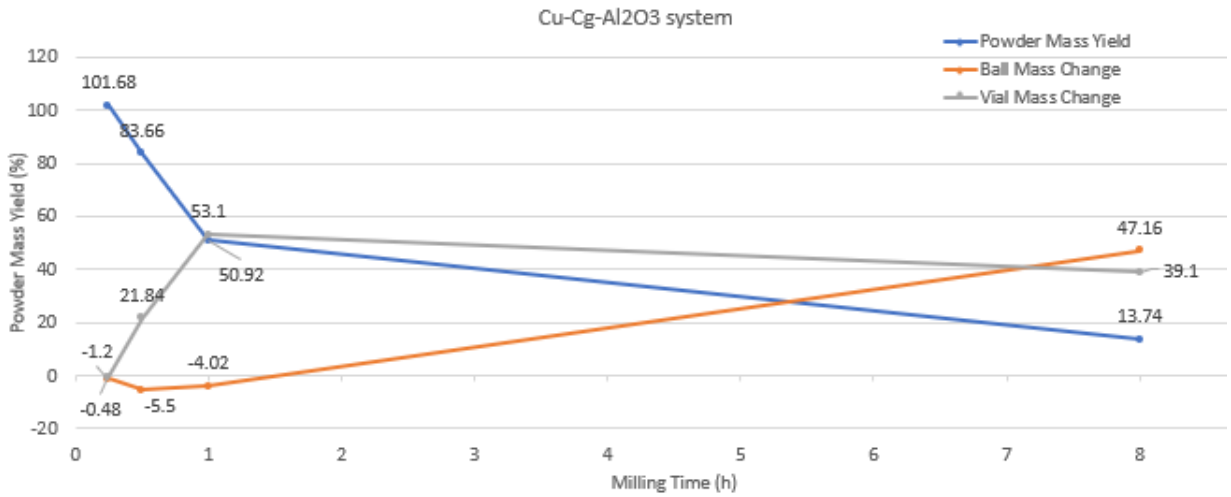

Figure 15- Powder Mass Yield changes during milling runs in the Cu-Cg-Al_2O_3 systems.

4.1.3. Copper – Graphite – Alumina – Silver System.

Figure 16 reports the effect of the of silver in the mass yield of the powder batches and on ball mass variation. The addition of silver increases the mass yield for all milling times when compared to the previous systems. Moreover, this increase in efficiency is most intense for longer milling times, which are the critical runs when it comes to mass yield decrease. The role of silver alloying in the increase of copper recrystallization temperature is well documented. This suggest that silver was effective in decreasing copper ductility, providing an increase in mass yield through enhancing the fracture frequency of the welded material. The change in process behaviour and increase in efficiency indicate the success of solid solution in the copper matrix. Longer milling time provides more ball impacts, increasing silver micro alloying extension in the copper powders. The solid solution extension provides a hardness increase (as will be discussed on section 4.5). The change in mass yield becomes more noticeable for longer milling times because alloying is occurring during the milling run, activating silver alloying and changing the powder properties over time.

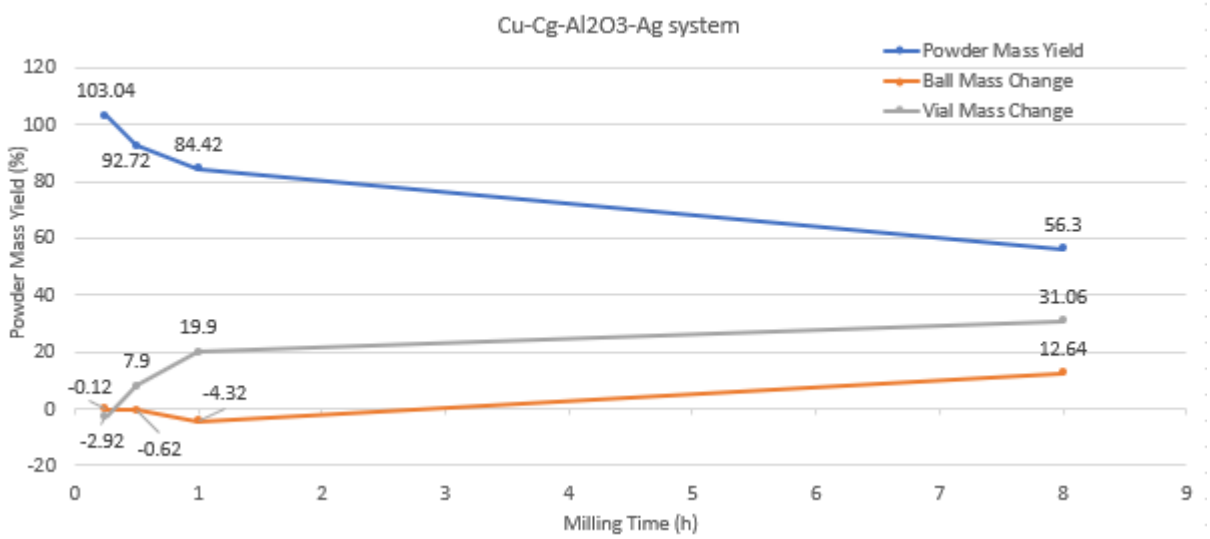

Figure 16 - Powder Mass Yield changes during milling runs in the Cu-Cg-Al_2O_3-Ag systems.

The increase in mass yield for the 8 h experiment, about 260%, was not expected. To confirm the validity of the result similar 8h experiments were carried out. These similar runs are in every aspect a repetition of the 8H experiment for the Cu-Cg-Al_2O_3-Ag system. Results obtained for powder mass yield and ball mass variation are presented in Figure 17.

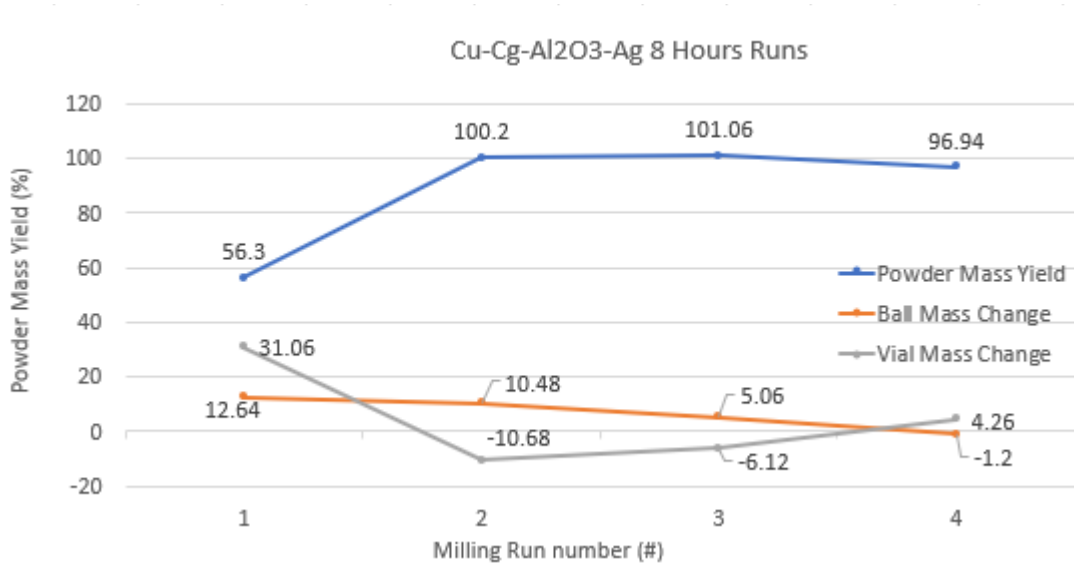

Figure 17- Powder Mass Yield changes during milling runs in the Cu-Cg-Al_2O_3-Ag system for different 8 hour runs.

The increased efficiency verified in the successive runs is not related to a change in the powder batch, as the experiments used the same methodology as the first run, but instead with the condition of the milling media. Run number 1 was the first performed milling experiment as previously described and also

shown in Figure 16. The following run, number 2, was performed after 1 hour, 30 minutes and 15 minutes runs to keep consistency, runs number 3 and 4 were performed after runs number 2 and 3 respectively. These runs were performed in a vial coated with all the material losses from all the previous runs. This milling media coating has demonstrated to increase the process efficiency by fracture. Just as seasoning a vial has showed to decrease the amount of contaminations in regular mechanical milling by coating the milling media with welded powder [47], the repeated experiments show that seasoning a vial is an effective method for increasing the process efficiency. The reason is that an uncoated milling media is prone to welding from the copper powders, while a coated milling media, while still able to weld, can provide the loose powder batch with fractured powder particles, effectively reducing the mass loss.

Furthermore, runs 2 through 4 matched the powder input and output, with around 100% powder mass yield. This result demonstrates that the fracture rate of cold worked powder welded onto the milling media matches the cold-welding rate and a steady state is achieved for mass flow. This result is achieved due to the double contribution of silver alloying; the increase in recrystallization temperature and powder hardness as well as the seasoning effect of the previous runs in the milling media surface.

4.1.4. Conclusions on mass yield of milling experiments with copper powders.

Copper powders tend to cold weld during milling, increasing powder size. This effect was reported for pure copper milling under air and protective atmosphere [107], during milling with carbon nanotube additions [108], and during milling with alumina additions [109]. However, no powder mass loss is reported due to copper welding taking place between same material powders, instead of the steel milling media.

However, previous synergic milling experiments with copper milling media evidenced that copper powders will weld to the milling media, decreasing the process efficiency [110].

Reduction of mass yield is a chief concern when milling ductile powders, especially for longer milling times. Long milling times provide the energy from ball impacts needed to enable the designed structural, morphological, and compositional changes in the powder; however long milling times also tend to lead to steady decrease of mass yield.

Different approaches were used to increase the milling run mass yield. The increase of strain hardening and decrease of powder ductility in order to increase fracture was the main strategy used. In the scope of the experiments carried out, the 2% addition of alumina was not effective in increasing the powder mass yield of the Cu-Cg-Al_2O_3 system when compared to the alumina free Cu-Cg system; instead, due to the effect on copper recrystallization temperature and solid solution hardening, significant improvement to the milled powder mass yield were observed after the addition of 1,6wt% silver, attaining a measured maximum yield increase of 260% relative to the previous maximum achieved in other systems for the 8h experiments.

Mass yield is also dependent on the milling run sequence. The more milling runs are carried out with un-reconditioned vial and balls the more the mass yield increases for any milling system; this is due to the accumulation of cold welded and cold worked powder in the vial walls and balls from previous runs that are more prone to fracture.

The use of silver alloying in Cu-Cg-Al_2O_3-Ag samples milled in tandem with a seasoned vial has shown to increase the process mass yield to 100%. This is considered a very promising result and might allow the use of previously non-viable low yield high milling rates.

4.2. Graphite particle size, defect content and amorphization

The present section describes the results for Raman spectroscopy: subsection 4.2.1. Provides an analysis of the main results obtained and their respective interpretation.

4.2.1. Graphite Amorphization Evolution

As previously referred in subsection 3.3.4, the evolution of the defect content and in the copper composite powders can be studied by the intensity ratio between the *D* peak, around 1300 cm^{-1}, and the *G*, around 1580 cm^{-1}. The *D* peak is activated when border defects are present in the carbon crystalline lattice and its intensity and broadening is thus related to the decreasing graphite crystallite size. The *G* peak reflects the degree of symmetry of the crystalline lattice and broadens with the decreasing distance between point defects in the carbon network [90,91]. The relationships between these peaks, either in intensity, area, or broadening describe the evolution of graphite defects in the milled powder samples.

The evolution of the intensity and width of the *D* and *G* peaks can be observed in Figure 18. The as-supplied graphite contains an intense narrow *G* peak and a weak characteristic *D* peak. As milling time increases, the *D* peak increases both in intensity and width, while the *G* peak becomes increasingly smaller and broader. Notably, although most changes introduced by milling, such as microhardness increase and crystallite size decrease, can be observed at the early stages of milling after 15m. The most visible changes in amorphous graphite content happen beyond 30 min milling.

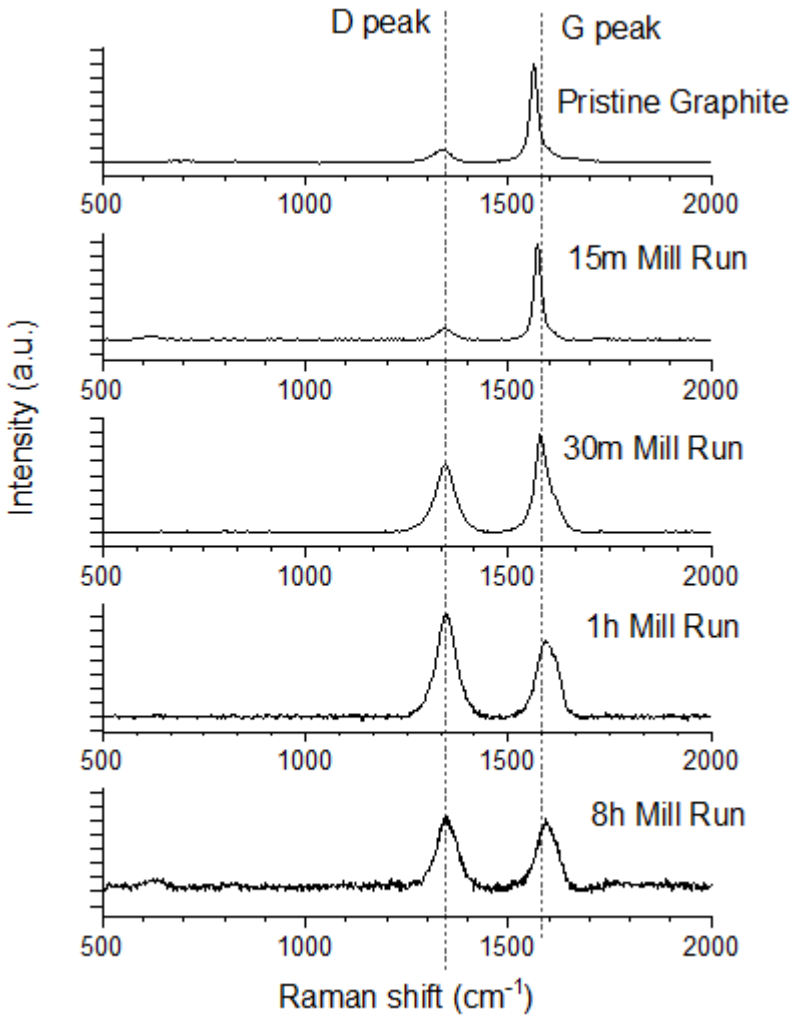

Figure 18 - Raman spectra for un-milled and milled graphite in the Copper Graphite composite system. G and D peaks are highlighted.

D and *G* peak intensity ratios Figure 19, *D* and *G* peak area ratios, Figure 20, and *G* peak broadening (FWHM), Figure 21, provide a scope on the evolution of graphite defects.

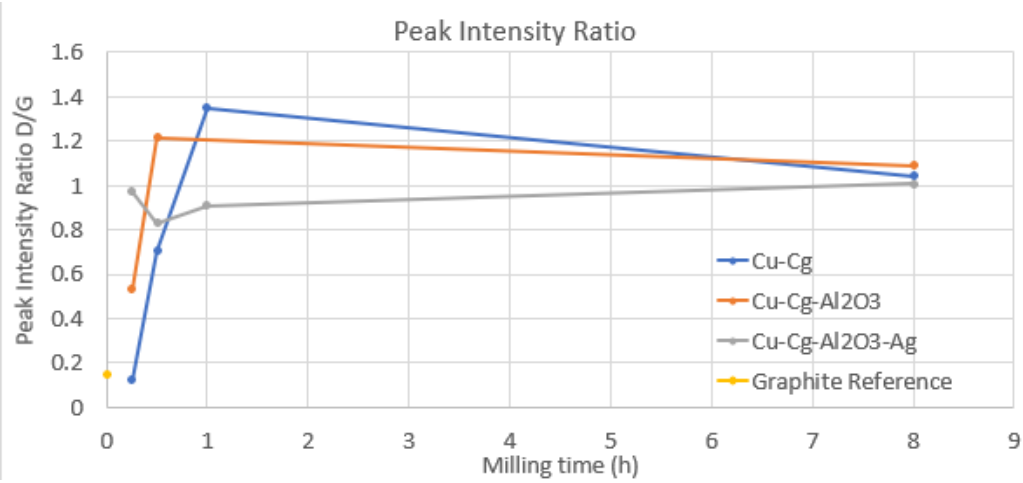

Figure 19 - Evolution over milling time of the ratio between the intensity of D and G peaks

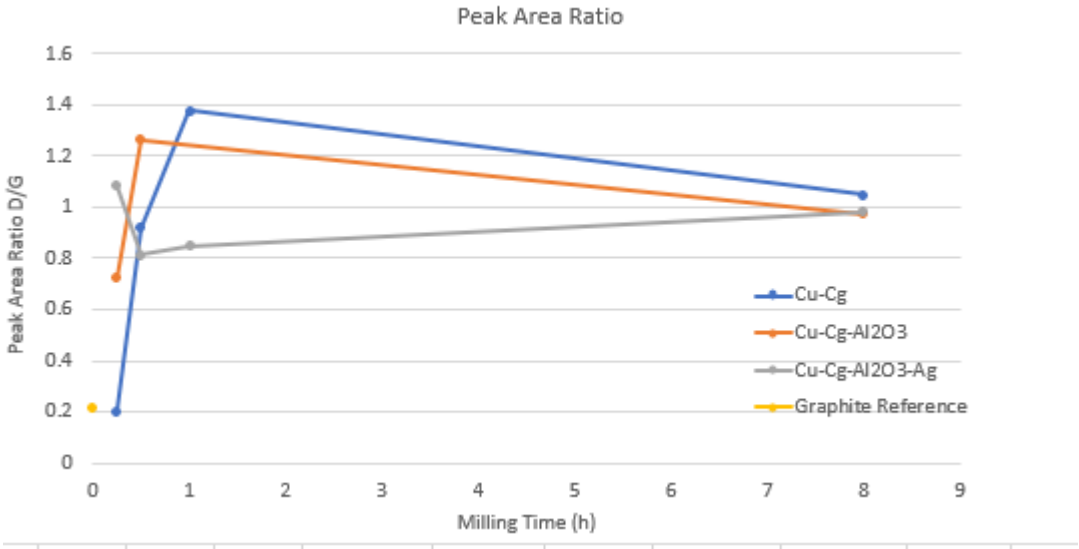

Figure 20 - Evolution over milling time of the area ratio between D and G peaks.

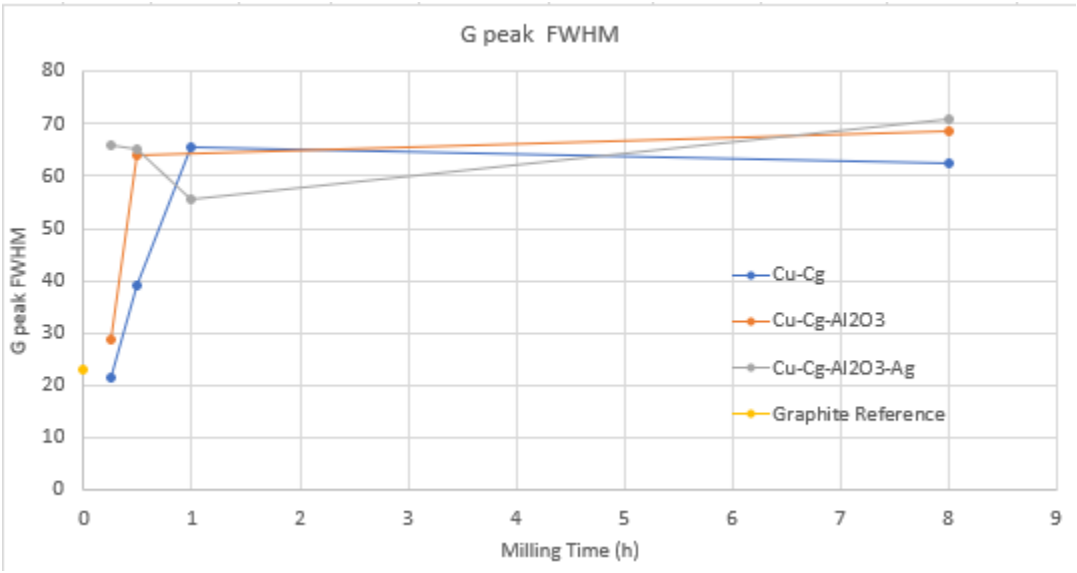

Figure 21 - Evolution over milling time of the G peak FWHM

The reported evolution of peak intensity ratios, area intensity ratios and *G* peak FWHM are all indicative of the initial stages of graphite amorphization [90,93,94]. However, amorphous graphite features a single broad band instead of the sharp G and D peaks, which is absent from the current Raman spectra.

Nevertheless these ratios provide critical information, peak intensity ratio can be used to quantify edge defects and calculate graphite crystallite size [90,91], peak area ration and G peak FWHM provide further information by quantifying point defects within the graphite lattice.

Graphite defect generation during milling is a process enabled by ball impact and appears to follow the same trends as the decrease in copper crystallite size or the increase in hardness. Most of the graphite defect content develops during the first hour of milling, and the amount of defects within graphite seem to evolve towards an asymptotic maximum which is reached after one hour of milling for most systems.

Both Copper-Graphite and Copper-Graphite-Alumina systems suggest a steady increase over time in defect content during the first hour of milling. Milling runs beyond 1h featured a decrease in *D* and *G* peaks intensity and area ratios, while the *G* peak FWHM increases in the Alumina system and decreases in the Graphite system.

The increase in the edge defects within graphite content suggests the increasing presence of finely subdivided small graphite crystallites. Smaller graphite crystallites provide a more effective contact wear behaviour, as edge surfaces are more chemically active, binding to atmospheric gases [26,28], and improve the graphite rich tribolayer lubricating properties [26,28]. Mechanical milling should provide increased wear properties for the copper composite through the decrease in graphite crystallite size.

4.3. Copper crystallite size, copper cell parameter shift and reinforcement peaks

X-ray results and analysis are covered over three subsections. Subsection 4.3.1 provides a qualitative analysis of the composite powder peaks. Each reinforcing element peak is identified and changes over time are reported. Section 4.3.2 provides a quantitative analysis of the composite copper peaks in order to report the crystallite size evolution. Trends and differences between systems are discussed. Subsection 4.3.3 provides a quantitative analysis of the composite copper peaks in order to report the lattice parameter evolution. The change in the lattice parameter is used to discuss the possibility of the different reinforcing phases forming a copper matrix solid solution.

4.3.1. X-Ray diffractometry

X-ray diffractograms were obtained and analysed using the methodology outlined in subsection 3.3.2. Obtained results are shown in Figure 22, Figure 23 and Figure 24, respectively for the Cu-Cg, Cu-Cg-Al_2O_3 and Cu-Cg-Al_2O_3-Ag systems. Quantitative analysis of these diffractograms is performed in the next two subsections, respectively 4.3.2 and 4.3.3. Besides copper peaks, diffractograms also contain Graphite, Alumina and Silver peaks in the appropriate systems. This holistic view of the milled powders provides a deeper understanding of the changes during the milling experiment, as well as a better critique of the results in section 4.3.3.

As referred, Figure 22 contains the X-ray diffractograms of the milled composite powder samples in the Cu-Cg system. As expected, peak intensity is strongly dependent on the phase content present in the powder sample, and thus, cfc copper peaks are more intense. The five peaks outlined in Table 11, used for calculating crystallite size can be clearly identified. A small graphite peak can be identified around 2θ =25º, for the 0.25h to 1h mill runs.

Copper peak broadening with higher milling times provides a qualitative visual representation of crystallite size reduction progress in the longer milling runs. Peak broadening, due to crystallite size reduction, is present in all milling systems and appears to follow a similar behaviour for all milling systems. The quantitative crystallite size analysis carried out in subsection 4.3.2 confirms this hypothesis. The graphite peak also broadens for milling times up to 1h and disappears for all 8h milling runs. This has been reported [86] to be caused by the increase in amorphous graphite content, which is expected the for the longest milling runs, and was confirmed by the Raman analysis on section 4.2.

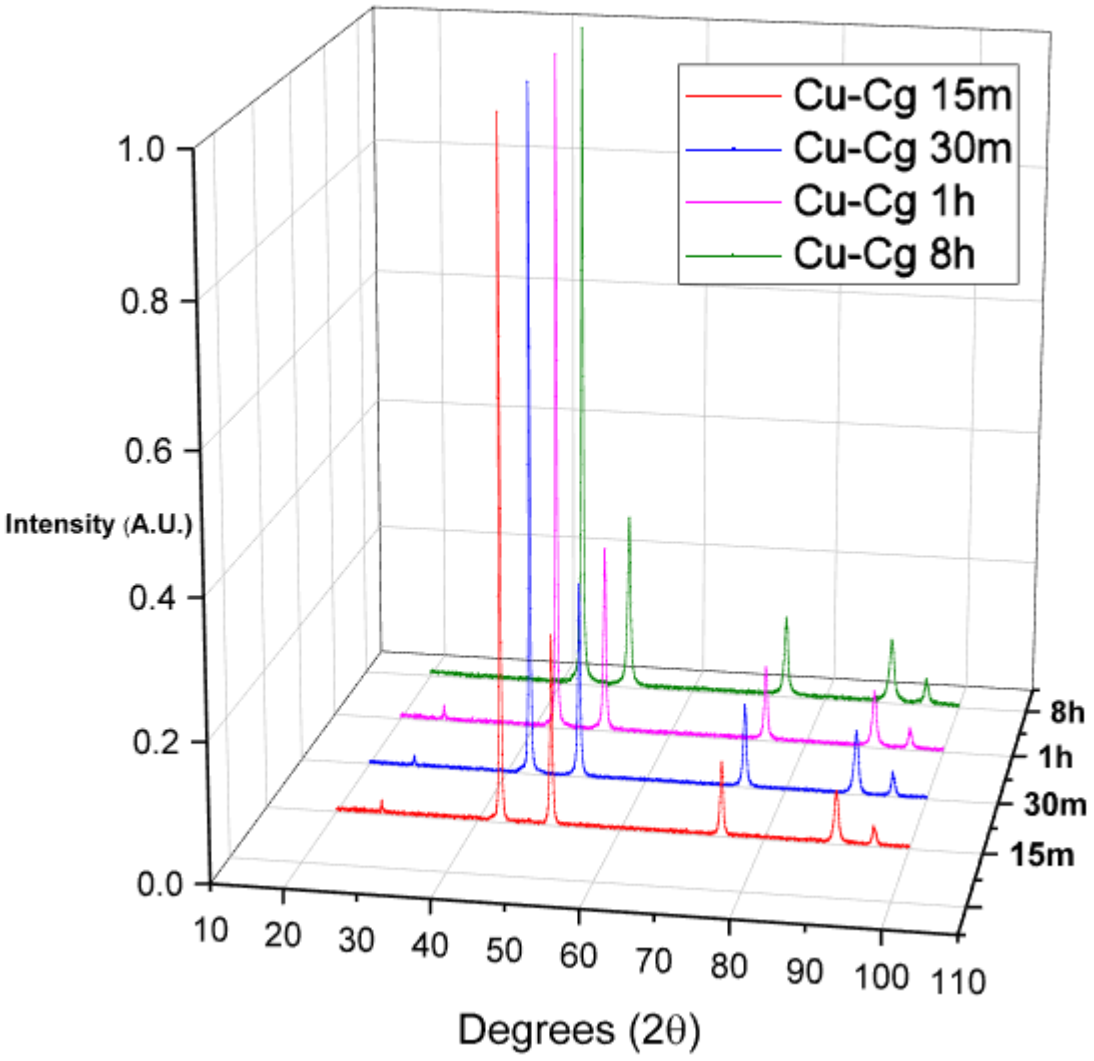

Figure 22 – X-ray diffractogram of milled powders in the Cu-Cg system.

Figure 23 contains the X-ray diffractograms of the milled powder composite samples in the Cu-Cg-Al_2O_3 system. In the diffractogram an alumina peak would be expected around 2θ=38º. However, no peak could be detected at that coordinate. This silent peak might be a consequence of the low alumina content in the powder batch and lower alumina peak intensity [86] .

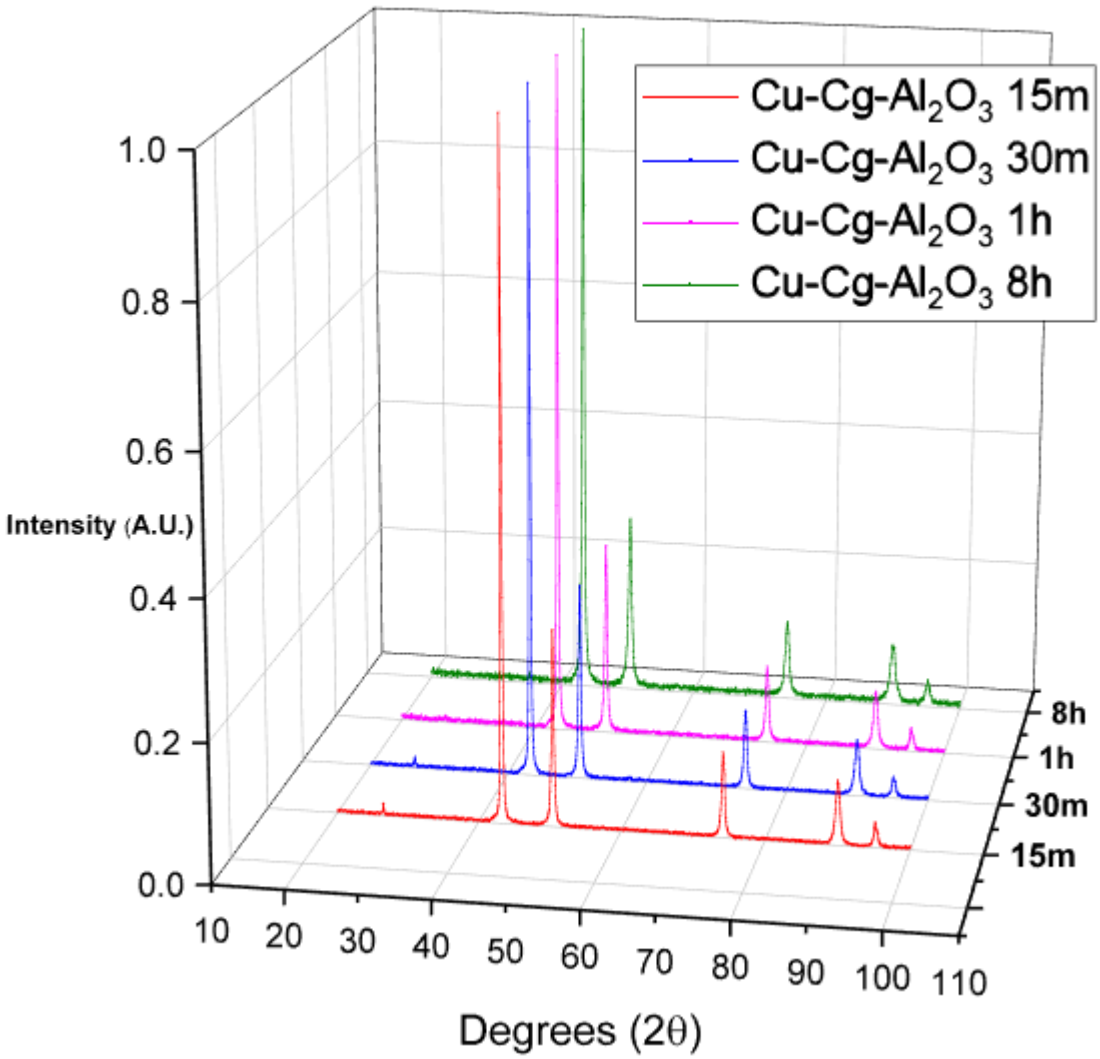

Figure 23 - X-ray diffractogram of milled powders in the Cu-Cg-Al_2O_3 system.

Figure 24 contains the X-ray diffractograms of the milled powder composite samples in the Cu-Cg-Al_2O_3-Ag system.

The most intense cfc silver peak, around 2θ =38º, is detected in all diffractograms up to 1 hour (including) milling, being absent after 8 hours of milling. The disappearance of cfc silver peaks after 8 hours milling suggests the formation of a copper cfc solid solution [46].

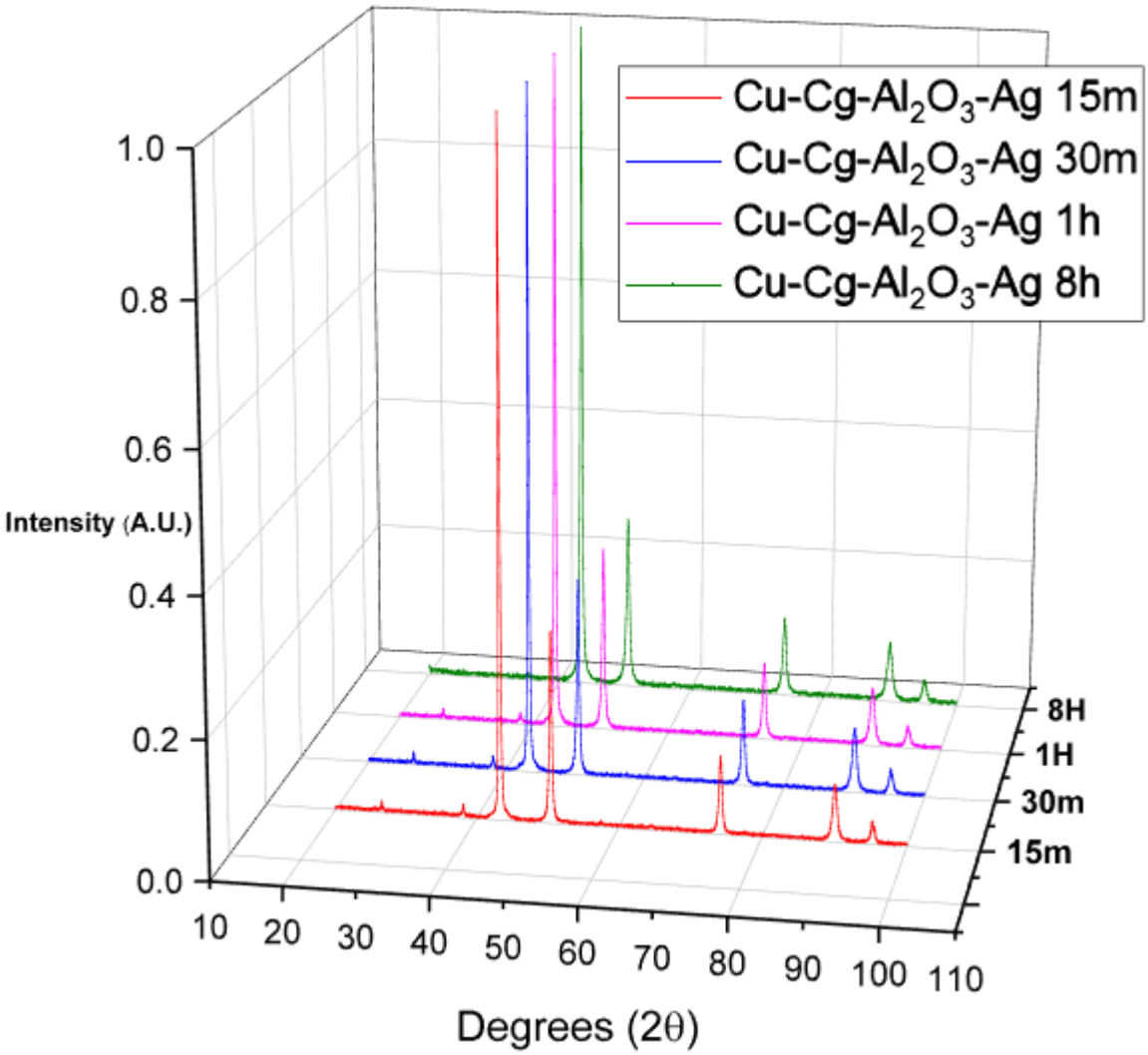

Figure 24 - X-ray diffractogram of milled powders in the Cu-Cg-Al_2O_3-Ag system.

4.3.2. Copper crystallite size evolution

Figure 25 illustrates the evolution of crystallite size over time in all milling systems, as well as that for a reference pristine copper sample. Crystallite size decreases with milling time indicating that the milling process is most efficient during the early stages of milling, featuring a decrease from approximately 60nm to 28nm in the first 15 minutes. Instead, the next 8 hours of milling only reduce the crystallite size to 20nm.

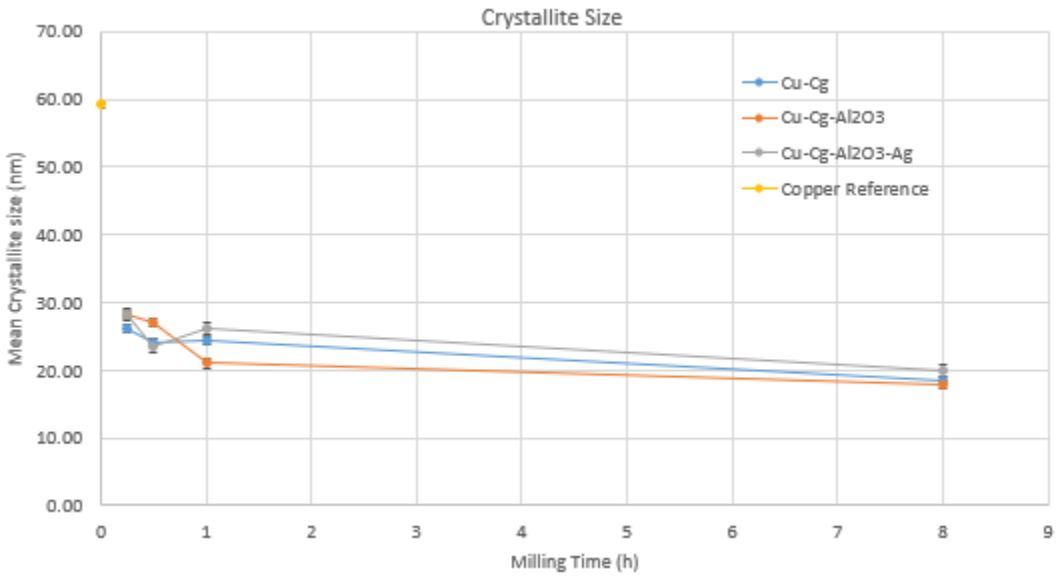

Figure 25 - Copper mean crystallite size evolution over milling time via Scherrer analysis, the crystallite size for unmilled powders -Copper Reference - is highlighted

Differences in crystallite size decrease trends in the different composite systems are negligible, as all observed systems present the same increased crystallite size reduction for early milling, followed by a celerity decrease for longer milling times. Crystallite size reduction is more efficient during the first 15 minutes of milling and achieves a similar small decrease, from 28nm-26nm to 20nm-18nm, after 8 hours milling.

However even slight decreases in crystallite size, at the nanometre scale, provide a large change in the contribution of Hall-Petch strengthening mechanism, and so the differences between systems featured in Figure 25 cannot be disregarded when discussing hardness increase comparisons.

Most surprisingly, silver alloying doesn't enable smaller crystallite sizes compared to the un-alloyed powders. This change is unexpected as the addition of silver increases copper recrystallization temperature, this effect is directly related to a decrease in crystallite size for milled Copper [48,111,112].

The internal strain contribution to the peak broadening could not be quantified as the Williamson – Hall method, despite providing sensible, did not feature good agreement in the linear regression, and no suitable R^2 values could be determined. This was also reported in similar works [53]. Therefore, all current peak broadening can only be interpreted based on the effect of crystallite size decrease.

4.3.3. Solid solution

Lattice parameter shifts are indicative of the occurrence of solid solution formation, as foreign atoms are introduced into the copper lattice. This evolution is dependent on the powder batch composition and milling run time.

Solid solution only occurs if there is compatibility between the copper lattice and the introduced atoms, as such not all systems observe this phenomenon, independently of milling time.

When discussing the occurrence of solid solution, it should be observed that the maximum lattice shift in proportional to the elemental powder batch composition. Consequently, small (such as 1.6wt% silver) soluble powder additions can only yield small lattice parameter shifts, which may fall within the method's estimated error [79,113].

Figure 26 illustrates the evolution of the lattice parameter over time in all the milling systems, as well as for a reference pristine copper sample. Lattice parameter shifts in Graphite and Alumina powder systems are within the method's estimated error and are not indicative of the occurrence of solid solution, which is in agreeance with the low solubility reported in copper [10, 27,114].

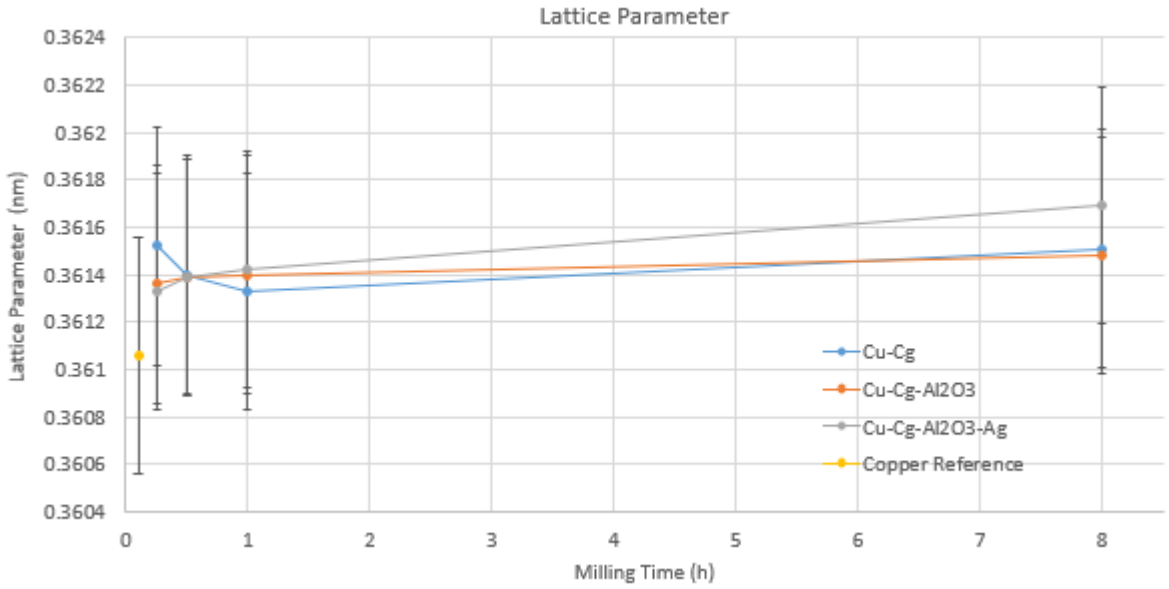

Figure 26- Lattice parameter change over milling time.

The silver system features a different behaviour, increasing linearly along time as per Figure 27. However, the increase in lattice parameter still fits inside the method's inherent error, the reason for the lattice parameter limited increase is an inherent consequence of the powder composition. An addition of 1% silver can only provide a proportional lattice parameter shift. Using Vergard's law [42,115] it is possible to estimate the maximum lattice parameter that is achievable for high milling times. However, even this calculated value, 0.36196 nm, falls within the estimated method's error.

Even without a lattice parameter shift wide enough to be expressed over the method's inaccuracy, the linear increase of the lattice parameter along milling time and the change in powder mass loss behaviour indicate that the addition of silver to the powder batch does in fact affect the copper powder behaviour. In order to obtain clear solid solution evidence, lattice parameter shift must be evaluated in systems with an

increased solute content. However, the eventual disappearance of silver peaks for longer milling experiments featured in Figure 24. Beyond X-ray diffraction, other characterization techniques also support the existence of solid solution. These results clearly support the occurrence of the formation of a solid solution of Silver in Copper.

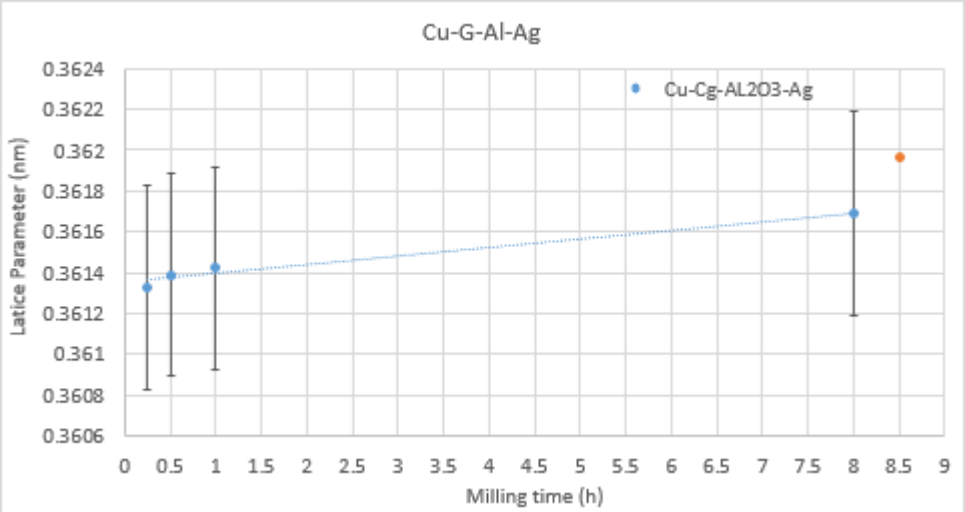

Figure 27 - Lattice parameter increase over time in the Silver system, the maximum lattice parameter shift according to Vergard's law is highlighted

4.4. Powder shape, size and microstructure evolution

This section focuses on the obtained Scanning Electron Microscopy images of the powders cross sections delivering a critical evaluation of the metallographic structure of the powder samples. Due to limited access to the SEM machines only the Cu-Cg system was studied.

4.4.1.The Cu-Cg system

Powder welding and size increases with milling time was a ubiquitous phenomenon. As hinted by the milling mass experiments, in the Cu-Cg system, no steady state where cold worked powder fracture matches the welding rate was achieved for any milling time. As a result, powder size increases along milling time.

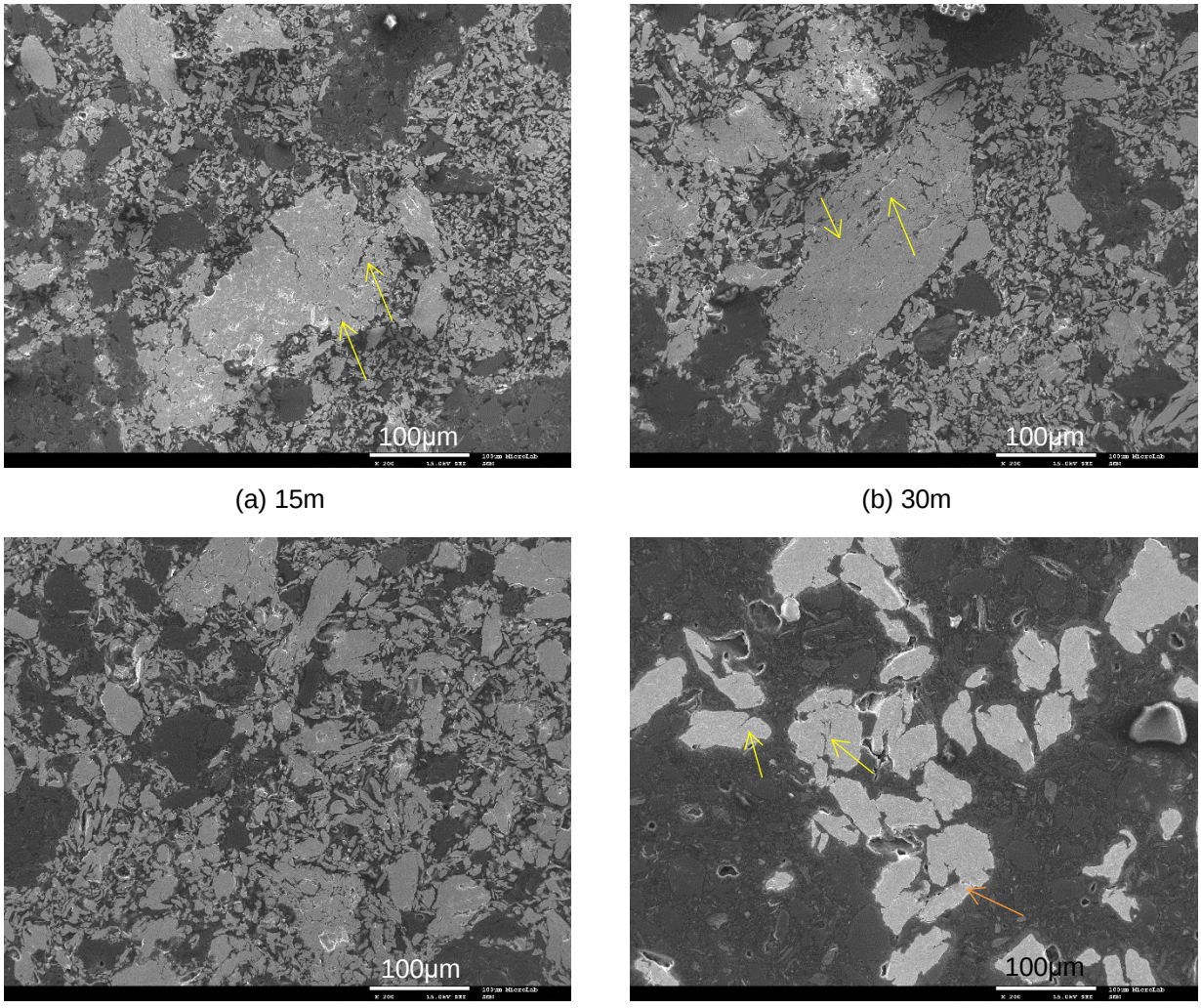

(a) 15m (b) 30m

(c) 1h (d) 8h

Figure 28 – SEM Micrograph of Cu-Cg milled powders.

For short milling times, Figure 28 (a) and (b), powder size is clearly inhomogeneous, with an apparent bimodal distribution. The origin of this bimodal distribution originates from the presence of both small powders featuring a limited amount of welds and large powders with a large amount of welds. Most of the powders seem to have a very small size. At the utmost larger spectrum of the distribution, some very large powders can be found, with sizes greater than 200 µm.

These large grains contain a pattern of cracks along the cross section (yellow arrows). Smaller powders correspond to copper powders with a small number of welds, retaining a size close to the initial powder size, in the order of 10-50µm, while the big powder particles seem to be formed from multiple welded powders with cracks displaying unwelded surfaces. Further milling, Figure 28 (c) and (d), reveals a tendency towards size homogeneity. Figure 28 (c) shows that most smaller powders have grown by cold-welding, possessing now a larger average size than the initial one, for the smaller powders. Also, the previous very large powders seem to have fractured, and only powders in the order of 100 µm could be observed at this stage. This seems to indicate that large cold-welded powders become cold worked and

fracture after 1h milling. Lastly, Figure 28 (d), at 8 hours milling no unwelded copper powders remain and the very large cold-welded powders have fractured down, resulting in a monomodal size distribution, with an average grain size around 50 μm. Powders are much more compact and its shape is more isomorphic. Some cracks are still visible inside the powders (yellow arrows) and same big voids (orange arrows), resulting from welding of larger powders and characteristic of ductile metal powder milling [46,116], are also visible. This may indicative that a steady state powder size was attained with the same rate of powder cold-welding and fracture.

Powder microstructure and shape is further explored in higher magnification SEM micrographs (Figure 29).

After 15 minute milling, Figure 29 (a), some smaller powders still present a remnant of its original dendritic shape (green arrows), while, at the same time, agglomeration and cold-welding between small deformed powders is clearly evident, evidenced by voids (orange arrows) and cracks or incomplete weldments (yellow arrows). Larger powders (Figure 29 (b)) have rounder or flake like shapes, as a result from multiple agglomeration and cold-welding between smaller powders or clusters. Multiple voids (orange arrows) and cracks (yellow arrows) are visible in these powders. This suggests that the powder growth mechanism is deformation under impact, agglomeration and progressive cold-welding of the powders.

Layered flake like structures develop as milling progresses. Work hardening, fracture and cold-welding intensifies under long milling times, with welded interfaces being visible due to etching contrast. As powders get welded and flattened repeatedly, they decrease in size, the welded layers became thinner and the number of weld lines increases.

Welded powders in Figure 29 (c)-(e) and (h), which feature the 30 minute and 1 hour samples, contain a large amount of cracks which represent uncomplete welds. Longer milling times featured in Figure 29 (f) and (g), featuring the 8h milling sample are more compact with the cracks having origin in cold work fracture instead of unwelded surfaces, as they seem to cross through cold-welded layers. Backscattered electrons images Figure 29 (g) and (h) show graphite particles (red arrows), and illustrate their successful dispersion inside copper grains, which is key in enabling the creation of a lubricating tribolayer [32].

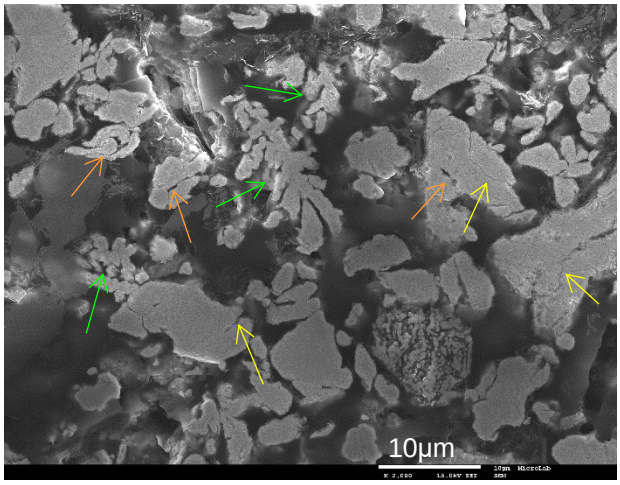

(a) 15m

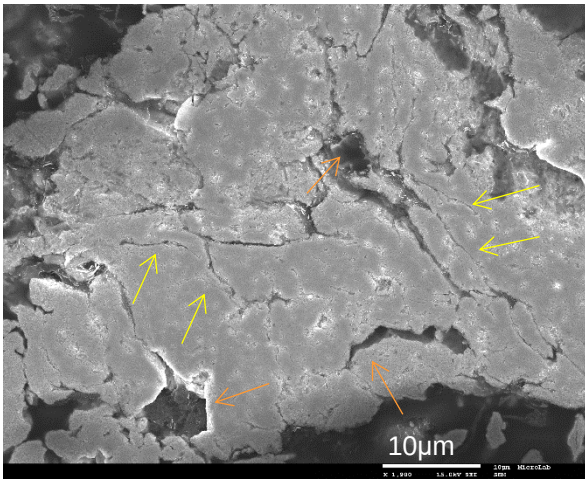

(b) 15m

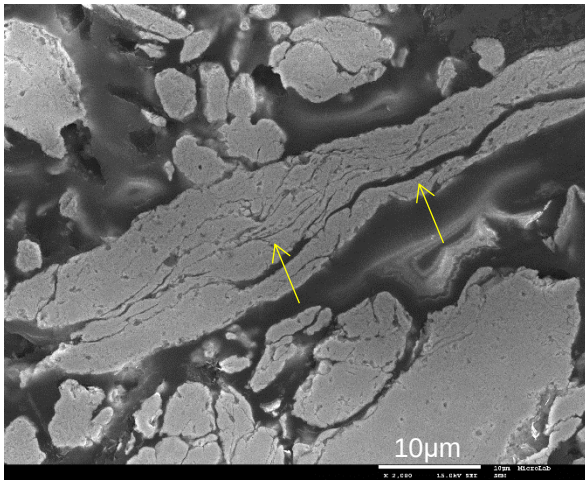

(c) 30m

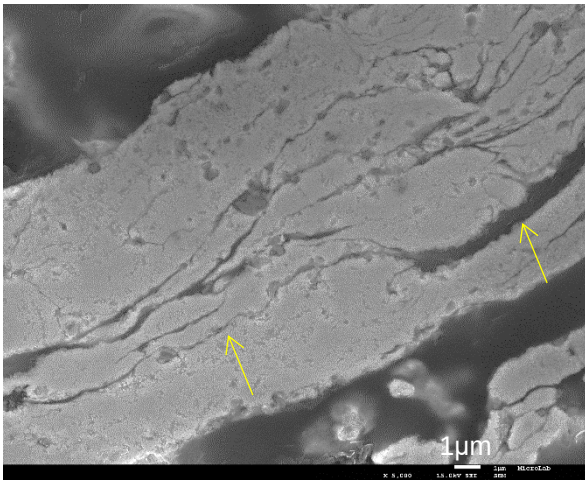

(d) 30m

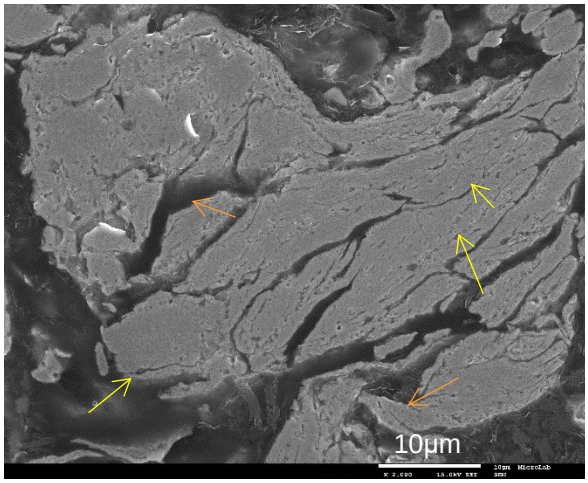

(e) 1h

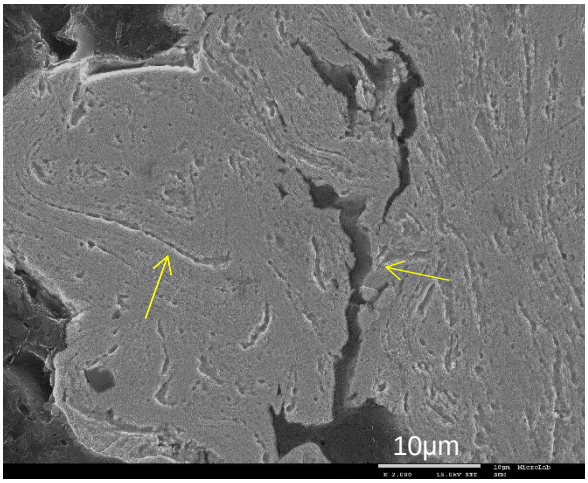

(f) 8h

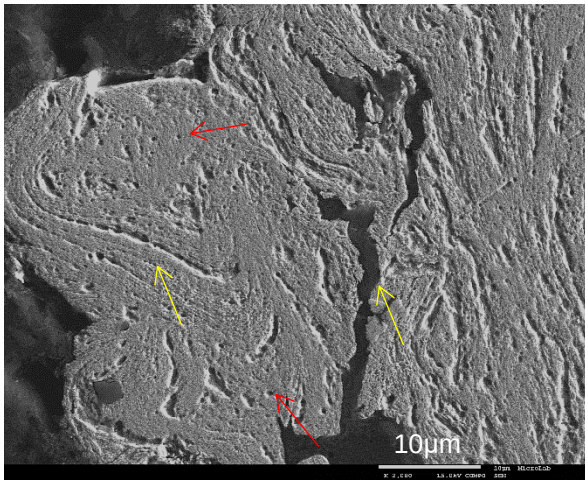

(g) BSE 8h

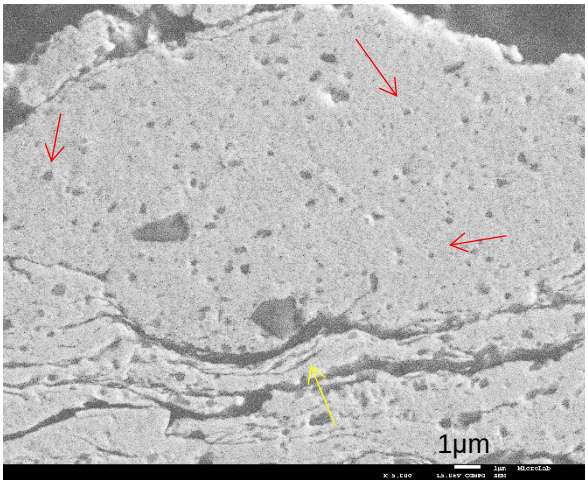

(h) BSE 30m

Figure 29 – SEM Micrograph of Cu-Cg milled powders. Figures (g) and (h) are obtained under BSE. Arrows are colour coded : Yellow – crack incomplete welds; Orange – Voids; Green – dendritic shaped powders; Red – graphite particles.

4.5. Powder Hardness via Deep Sensing Indentation – Ultra Micro-Hardness

This section presents the main results obtained by powder ultra micro-hardness testing via deep sensing indentation. The results provide a comparison between the different powder systems in order to understand the impact of milling time and the role of each reinforcement in the composite hardness. Obtained results are shown in Figure 30, also displays values for Copper Reference.

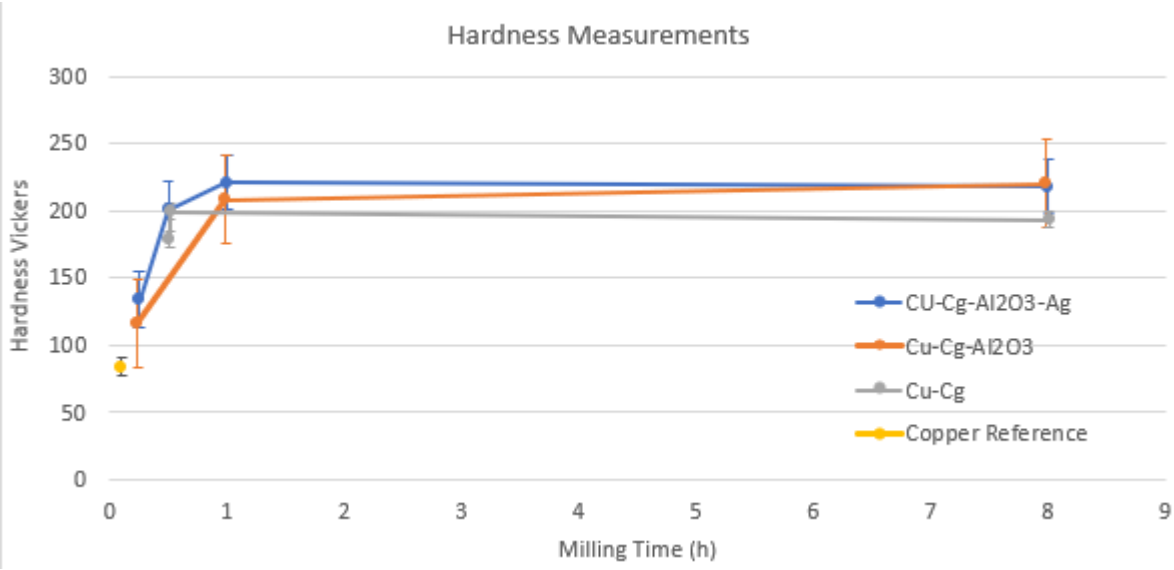

Figure 30 - Evolution of powder hardness over time, the standard hardness is highlighted

Several factors increase the powder hardness when compared to the used electrolytic copper standard that displayed 80 HV0.025. The total matrix hardness can be interpreted as the cumulative hardness provided from all strengthening mechanisms [116]. The considered mechanisms are: the intrinsic copper lattice hardness, constant for all systems as it is a feature of copper; work hardening of the copper matrix that can provide hardness values up to 120HV [117]; Orowan strengthening because, as milling progresses, smaller particle sizes are achieved and small dispersed particles, below 100nm, provide an obstacle do dislocation motion, increasing composite hardness; Hall-Petch strengthening contributes to composite hardness, due to decreasing crystallite size developed during milling; silver solid solution strengthening due to the increase of silver solubility in the copper structure along milling; second phase reinforcement, through a load sharing rule of mixtures, as hard dispersed particles act as a physical reinforcement of the composite.

Hardness increases due to the composite powder composition, as different powder additions either enable or increase an already present hardening mechanism. This increase can be observed when comparing the different systems. Hardness also increases along milling time, as longer milling times either enables or increase an already present mechanism. This increase can be observed when comparing the different milling time.

In the case of different powder compositions:

- The Cu-Cg system may enable Orowan strengthening as graphite particles dispersed over the copper matrix reduce their size being an obstacle to dislocation motion. Small graphite particles, Figure 29(g), are reported to be contained inside copper powders. A possible second phase reinforcement could be considered for the Cu-Cg system. However weak affinity between the copper and graphite interface limits the possible load transfer between the matrix and the reinforcement. Also, the render soft nature of

graphite also limits the second phase reinforcement mechanism. This contribution, in the case of the Cu-Cg system, has been considered negligible [118].

- The Cu-Cg-Al_2O_3 system foster an increase Orowan strengthening mechanism, as it features both graphite and alumina particles dispersed over the copper matrix. Furthermore, alumina particles feature a smaller starting grain size and brittle fracture behaviour, providing a final smaller particle size. The previously negligible second phase reinforcement mechanism is enabled due to the high hardness and bonding of the alumina particles.

- The Cu-Cg-Al_2O_3-Ag system, beyond the already referred mechanisms, enables solid solution strengthening. This effect is activated by milling and is expected to be more intense for longer milling runs as the oversaturated Cu-Ag solid solution develops.

In the case of different milling time:

- The work hardening contribution increases, as the cumulative powder deformation increases. A maximum value to the work hardening hardness contribution in copper is found for heavily cold worked copper [117].

- Orowan strengthening is expended to increase, as two key conditions are developed during milling. Particles, either graphite or alumina, get dispersed inside the copper powders and particle size decreases. Overall, longer milling increases the particle availability inside copper powders and reduces their average particle cycle both contributing to Orowan strengthening.

- Hall-Petch strengthening is increased with milling time as the copper crystalline structure gets refined. This contribution can be calculated from the copper mean crystallite size.

- Solid solution strengthening increases in the Cu-Cg-Al_2O_3-Ag system, as the silver phase is progressively dissolved into the copper structure.

Table 12 provides the mean hardness values for each system:

Table 12 – Powder's mean ultra-microhardness values.

Milling time / System	15 min	30 min	1 h	8 h
	Hardness Values (HV0.025)			
Reference Cu	84±6			
Cu-Cg	-	179±18	199±18	193±13
Cu-Cg-Al_2O_3	116±12	-	208+17	220±27
Cu-Cg-Al_2O_3-Ag	134±12	201±21	221±8	218±17

To comprehend each contribution to hardness increase a step by step analysis is carried out:

The Cu-Cg 30m powder features a hardness of 179 HV. The hardness contribution to this system can be divided into: intrinsic copper hardness (30HV) [113,119], copper crystallite size hardening (26nm;250HV) [113,119]. Cold working of copper grains is expected to contribute with an hardness increase around 60 HV [117]. Orowan strengthening from dispersed graphite grains probably features a small contribution due to the initial particle diameter (d_{50}=2.4μm). This tentative estimation of powder hardness yields an expected hardness of 340 HV. While some values are overshoot, crystallite size is

higher than 26nm due to Scherrer method's inability to separate strain broadening from grain size broadening. However, even for small milling times the biggest contribution to composite hardness is grain size refinement.

The Cu-Cg composite powders milled for 1 and 8 hours respectively saw an increase in hardness, this increase can be attributed to a further refinement in the grain structure. The 8h composite featuring the smallest Crystallite mean size does not feature the highest hardness.

The Cu-Cg-Al_2O_3 system enables two more hardening mechanisms beyond those active in the Cu-Cg system. The end result is an higher overall hardness for all milling times. Load sharing of alumina provides a maximum hardness increase around 4 HV due to the small (4%) volume occupied by alumina particles inside the composite powders. Orowan strengthening provides the additional increase in comparison with the Cu-Cg system. Orowan strengthening is expected to increase along milling time: this effect is confirmed by the increasing hardness difference between the Cu-Cg and Cu-Cg-Al_2O_3 systems, which is 9 HV and 27 HV, respectively for 1h and 8h milling, despite a similar rate of crystallite size reduction.

The Cu-Cg-Al_2O_3-Ag system enables solid solution strengthening, this contribution is expected to increase along higher milling times, as solid solution during milling runs is an impact activated process. This effect is confirmed by the gradual increase in the lattice parameter along milling times reported in Figure 26. However, the biggest increase in the Cu-Cg-Al_2O_3-Ag in relation to Cu-Cg-Al_2O_3 system is found at 15m, suggesting that silver solid solution happens at short milling times and with significant increase (18HV). The relative decrease in the Cu-Cg-Al_2O_3-Ag system hardness is caused by higher crystallite mean sizes, which decrease the Hall Petch contribution.

Overall, while this work demonstrated that both powder composition and milling time induce hardness increase, it is grain refinement, enabled by longer milling runs, that provides the greater contribution. However, diminishing returns can be observed in the hardness increase after 1 hour milling, as the hardness seems to reach an asymptotic limit. This phenomenon is related to the decrease of crystallite size for longer milling times as shown in Figure 25. In the Copper – Graphite and Copper – Graphite - Alumina systems hardness results indicate that 1h milling is the ideal milling time to avoid unnecessary mass losses. However, the Copper – Graphite - Alumina - Silver system can effectively minimize powder mass losses and make available longer milling times. However, no relevant hardness increase is expected to happen after 8H milling when working with 200RPM.

Additionally the hardness increase due to solid solution, which is an important contribution in the Cu-Cg-Al_2O_3 system, allows to infer the existence of solid solution.

Chapter 5. Conclusions and Future Work

This chapter provides a closure to the thesis work. It addresses the unfinished work in section 5.1. The main findings and conclusions of this work are presented in section 5.2. Section 5.3 aims to provide possible future routes of investigation to further developed the work of this thesis.

5.1. Unfinished work

Due to the sanitary emergency lockdown, further experiences were cancelled, the following section features the interrupted work, along with their relevance and expectations:

5.1.1. Temperature influence on powder properties

In order to predict if sintering was a viable process for producing bulk nanocrystalline composites, powders from all milled systems would be test annealed in the 500ºC - 900ºC, and particularly in the 800ºC - 900ºC, under a reductive Argon-Hydrogen atmosphere. The powders would be characterized by X-ray diffraction, Raman spectroscopy and hardness testing, in order to quantify the temperature enabled evolution of powder properties upon annealing. Critical points of analysis would be the success of the dispersed alumina and graphite particles in decreasing grain size growth and the role of silver in grain growth kinetics.

Consolidation techniques must be designed to achieve a balance between the increase of apparent density and coarsening of the structure.

5.1.2. SEM analysis

In order to better understand the microstructural and alloying effects of the addition of the different elemental powders, Scanning Electron Microscopy would be carried out in all powder compositions. Samples would be analysed in increasing order of composition complexity. Due to the lab closing, only the simplest system, Cu-Cg was analysed.

The powder systems would be photographed and analysed in order to find differences and similarities in powder welding, fracture and the consequent powder size evolution over time. Critical points of analysis would be; the effect of powder composition in the welding and fracture behaviour of powder particles; the alumina particle size and localization evolution with milling time in order to address grain boundary pinning and hardness gains by oxide dispersion strengthening; and composition maps in regard to silver distribution in the composite powders.

5.2. Conclusions

Several experiments were performed in order to produce contamination free copper composite powders using the synergic milling route. To avoid oxidation of the metal powders processing and handling were carried out under a high purity Argon atmosphere with an Oxygen and H_2O content below

0,1 ppm. Powders were produced using 15m, 30m, 1H and 8H milling runs for various systems, with an increasing number of elements being added into the powder batch, respectively, Cu-Cg, Cu-Cg-Al_2O_3 and Cu-Cg-Al_2O_3-Ag. The compositions Cu-2wt%Cg, Cu-2wt%Cg-2wt%Al_2O_3, and Cu-2wt%Cg-2wt%Al_2O_3-1,6wt%Ag were selected.

The milling process efficiency was the main process bottleneck in the early stages of experimental procedure, with longer milling times resulting in low yield. Also, milling rates over 200 RPM, even short times, reduced process efficiency below the acceptable yield. This result was not observed in non-synergistic milling in air [107–110], and suggests that adhesion to the milling media and cold-welding is increased when working within oxide free synergic milling.

The use of 200 RPM milling rates featured an increase in process efficiency over an acceptable threshold for characterization for all milling times. However, the chief reason for process yield increase was the addition of silver to the powder batch, opening the possibility of enabling higher milling rates.

Electrolytic copper powders start with a dendritic shape. Through cold-welding the powders start growing and forming layered powders with a bimodal distribution, featuring both large sized welded powders and small powders with few welds. After 1 hour milling, cold worked powders fracture and powder size becomes less inhomogeneous. Average powder size grows over time during all the milling runs.

Solid solution between copper and silver in mechanical milling increases composite hardness and reduces ductility. This effect changes powder mass transfer behaviour, increasing the process mass yield. Solid solution is difficult to characterize for low solute contents; however, x-ray diffraction shows the suppression of silver peaks and a lattice parameter increase, particularly from 1 hour to 8 hours milling. The additional change in composite properties, such as a hardness increase, and the change in mass transfer behaviour are indicative of a successful solid solution.

While alumina and silver additions increase the composite hardness, work hardening and crystallite size reduction appears to play a major role in hardness increase. However, additions are still relevant in order to provide composite performance and enable milling in the case of silver.

In terms of accomplished goals, the production of MMC copper composites with graphite and alumina reinforcing phases and combinations thereof, as well as silver alloying was successful. A successful employment of the synergic milling approach to reducing contamination during the milling process and tackling the inherent challenges of synergic milling approach is reported. No contamination was found in the copper composites either by X-ray diffraction or EDS analysis. Silver composites also achieved high milling mass yields. An increase in powder hardness is reported, with the maximum value of 220 HV both in the Cu-Cg- $Al_2O_3$and Cu-Cg- Al_2O_3-Ag systems. This result is far from the projected 300HV, but is nonetheless higher than the available values for work hardened copper, which shows that high energy milling is an effective method of increasing copper hardness by creating a nanostructured composite matrix [117], and is higher (or comparable in the case of systems with and higher alumina wt%) than most values reported under previous work milling for ODS copper via high energy mechanical milling [17,18,23–25]

5.3. Future work

The presence of unfinished work and the conclusions drawn from the milling experiments allow the following suggestions for further work:

Use of silver microalloying and sacrificial milling runs to increase the process efficiency, allowing the use of higher milling rates, in order to increase process energy, enabling further reduction of crystallite and alumina particles sizes, with the main goal of further increasing hardness.

Quantification of grain growth and hardness decrease under sintering temperatures, in order to select the optimal sintering temperature and time conditions. Similarly, sintering processes must be employed in order to study the stability of silver solid solution and infer the study the possible formation and nature of silver precipitates.

Producing Sintered composites, in order to characterize density and electrical conductivity properties, along with a tribological study of wear behaviour.

A comparison of composite properties with an increased content of silver alloying, based on the principle that solid solution is viable for any powder composition

Transmission electron microscopy analysis were already requested for the composite powder samples in order to study crystallite size, particle dispersions, the nature of silver alloying and the occurrence of absence of silver precipitates.

Chapter 6. Bibliography

1. Nunes D, Correia JB, Carvalho PA, Shohoji N, Fernandes H, Silva C, et al. Production of Cu/diamond composites for first-wall heat sinks. Fusion Eng Des. 2011;86(9–11):2589–92.
2. Carvalho PA, Fonseca I, Marques MT, Correia JB, Almeida A, Vilar R. Characterization of copper-cementite nanocomposite produced by mechanical alloying. Acta Mater. 2005;53(4):967–76.
3. Decker F, Harker D. Recrystallization in rolled copper. Trans Aime. 1950;188(June):887–90.
4. Dias M, Antão F, Catarino N, Galatanu A, Galatanu M, Ferreira P, et al. Sintering and irradiation of copper-based high entropy alloys for nuclear fusion. Fusion Eng Des. 2019;146(March):1824–8.
5. Hussain Z, Kit LC. [1] Z. Hussain and L. C. Kit, “Materials & Design Properties and spot welding behaviour of copper – alumina composites through ball milling and mechanical alloying,” vol. 29, pp. 1311–1315, 2008.Materials & Design Properties and spot welding behaviour of . 2008;29:1311–5.
6. Charde N. Exploring the electrodes alignment and mushrooming effects on weld geometry of dissimilar steels during the spot welding process. Sadhana - Acad Proc Eng Sci. 2014;39(6):1563–72.
7. Deshpande PK, Lin RY. Wear resistance of WC particle reinforced copper matrix composites and the effect of porosity. Mater Sci Eng A. 2006;418(1–2):137–45.
8. Kuntsche J, Schuster M, Schneider J. Engineering design of laminated safety glass considering the shear coupling: a review. Glas Struct Eng. 2019;4(2):209–28.
9. Harris SJ. Metal matrix composites. Vol. 35, Composites Science and Technology. 1989. 1–5 p.
10. Groza JR, Gibeling JC. Principles of particle selection for dispersion-strengthened copper. Mater Sci Eng A. 1993;171(1–2):115–25.
11. Ibrahim IA, Mohamed FA, Lavernia EJ. Particulate reinforced metal matrix composites - a review. J Mater Sci. 1991;26(5):1137–56.
12. Ying DY, Zhang DL. Processing of Cu – Al 2 O 3 metal matrix nanocomposite materials by using high energy ball milling. Mater Sci Eng. 2000;286(1):152–6.
13. ASM Handbook: Powder Metal Technologies and Applications. 9th ed. Vol. 7. 1988. 2148–2191 p.
14. Wang T, Zhang Y, Li G, Ma C, Xiao W. Effects of Al Content on the Physical Properties of Al2O3 Dispersion-Strengthened Copper Alloys. 2018;827–34.
15. Zhan Y, Zhang G. Graphite and SiC hybrid particles reinforced copper composite and its tribological characteristic. J Mater Sci Lett. 2003;22(15):1087–9.
16. Benjamin JS. Dispersion strengthened superalloys by mechanical alloying. Metall Trans. 1970;1(10):2943–51.
17. Rajković V, Erić O, Božić D, Mitkov M, Romhanji E. Characterization of dispersion strengthened copper with 3wt%Al 2 O 3 by mechanical alloying. Sci Sinter. 2004;36(3):205–11.

18. Rajkovic V, Romhanji E, Mitkov M. Characterization of high-energy ball milled prealloyed copper powder containing 2.5 wt%Al. J Mater Sci Lett. 2002;21(2):169–73.
19. England G. Hardness Scale Conversion Table Approximate Equivalents of Hardness Scales for Soft Metals [Internet]. 2018.
20. Totemeir WFGTC. Smithells Metals Reference Book. Vol. 1, Synthesis (Germany). 2004. 22–26 p.
21. Hahn SI, Hwang SJ. Estimate of the Hall-Petch and Orowan effects in the nanocrystalline Cu with Al2O3 dispersoid. J Alloys Compd. 2009;483(1–2):207–8.
22. Hwang SJ, Lee JH. Mechanochemical synthesis of Cu-Al 2 O 3 nanocomposites. Mater Sci Eng A. 2005;405(1–2):140–6.
23. Zhou D, Zhang D, Kong C, Munroe P, Torrens R. Grain and nanoparticle coarsening of an ultrafine structured Cu-5 vol.%Al2O3 nanocomposite during isochronal annealing. J Alloys Compd. 2015;642:83–91.
24. Rajkovic V, Bozic D, Popovic M, Jovanovic MT. The influence of powder particle size on properties of Cu-Al 2O3 composites. Sci Sinter. 2009;41(2):185–92.
25. Yan P, Lin C, Cui S, Lu Y, Zhou Z, Li Z. Microstructural features and properties of high-hardness and heat-resistant dispersion strengthened copper by reaction milling. J Wuhan Univ Technol Mater Sci Ed. 2011;26(5):902–7.
26. Braunovic M, Myshkin NK, Konchits V V., Myshkin NK, Konchits V V. Electrical Contacts: Fundamentals, Applications and Technology (Electrical and Computer Engineering). 2006;672.
27. López GA, Mittemeijer EJ. The solubility of C in solid Cu. Scr Mater. 2004;51(1):1–5.
28. Lee PK, Johnson JL. High-Current Brushes, Part II: Effects of Gases and Hydrocarbon Vapors. IEEE Trans Components, Hybrids, Manuf Technol. 1978;1(1):40–5.
29. A.Yli-Pentti. Comprehensive Materials Processing. Vol. 4, Comprehensive Materials Processing. Elsevier; 2014. 277–306 p.
30. Voort GF Vander. Metallography Principles and Practice. 1999. 560 p.
31. Moustafa SF, Ei-badry A. Effect of graphite with and without copper coating on consolidation behaviour and sintering of copper-graphite composite. Powder Metall. 1997;40(3):201–6.
32. Kováčik J, Emmer Š, Bielek J, Keleši L. Effect of composition on friction coefficient of Cu-graphite composites. Wear. 2008;265(3–4):417–21.
33. Moustafa SF, El-badry SA, Sanad AM, Kieback B. Friction and wear of copper – graphite composites made with Cu-coated and uncoated graphite powders. Wear. 2002;253(7–8):699–710.
34. Sadoun AM, Fathy A. Experimental study on tribological properties of Cu–Al2O3 nanocomposite hybridized by graphene nanoplatelets. Ceram Int. 2019;45(18):24784–92.
35. Rajkumar K, Aravindan S. Tribological behavior of microwave processed copper-nanographite composites. Tribol Int. 2013;57:282–96.
36. Rodrigues I, Guedes M, Ferro AC. Microstructural Changes in Copper-Graphite-Alumina Nanocomposites Produced by Mechanical Alloying. Microsc Microanal. 2015;21(1):120–31.
37. Pan Y, Lu X, Volinsky AA, Liu B, Xiao S, Zhou C, et al. Tribological and mechanical properties of

copper matrix composites reinforced with carbon nanotube and alumina nanoparticles. Mater Res Express. 2019;6(11).

38. Vitek JM, Warlimont H. The mechanism of anneal hardening in dilute copper alloys. Metall Trans A. 1979;10(12):1889–92.
39. Nestorovic S, Rangelov I, Markovic D, Nestorovic S, Rangelov I, Markovic D. Improvements in properties of sintered and cast Cu – Ag alloys by anneal hardening effect Improvements in properties of sintered and cast Cu – Ag alloys by anneal hardening effect. 2016;5899(April):35–9.
40. © Copper Development Association. Effect of various elements (impurities or intentional additions) on the conductivity of copper. 2018.
41. ASM International Handbook Committeee. ASM Speciality Handbook, Copper and Copper Alloys. 2001. 35–54 p.
42. Uenishi K, Kobayashi KF. Formation of a super-saturated solid solution in the Ag-Cu system by mechanical alloying. Mater Sci Eng. 1991;134:1342–5.
43. Kang N, Coddet P, Liao H, Coddet C. Cold gas dynamic spraying of a novel micro-alloyed copper: Microstructure, mechanical properties. J Alloys Compd. 2016;686:399–406.
44. Corrado J; TJC. Copper Trolley Wire and a Method of Manufacturing Copper Trolley Wire. 2000.
45. Imai THATK. Method of Producing G CU - AG Alloy Based Conductive Material. Vol. 1. 1996.
46. Suryanarayana C. Mechanical alloying and milling. Prog Mater Sci. 2001;46(1–2):1–184.
47. Koch CC. Synthesis of nanostructured materials by mechanical milling: Problems and opportunities. Nanostructured Mater. 1997;9(1–8):13–22.
48. Shen TD, Koch CC. Influence of dislocation structure on formation of nanocrystals by mechanical attrition. Mater Sci Forum. 1995;179–181:17–24.
49. Fecht HJ. Nanostructure formation by mechanical attrition. Nanostructured Mater. 1995;6(1–4):33–42.
50. Eckert J, Holzer JC, Krill CE, Johnson WL. Structural and thermodynamic properties of nanocrystalline fcc metals prepared by mechanical attrition. J Mater Res. 1992;7(7):1751–61.
51. Lu L, Lai MO, Zhang S. Diffusion in mechanical alloying. J Mater Process Technol. 1997;67:100–4.
52. Dadkhah M, Saboori A, Fino P. An overview of the recent developments in metal matrix nanocomposites reinforced by graphene. Materials (Basel). 2019;12(7).
53. Samuelson PA, Nordhaus WD. Economics nineteenth edition [Internet]. 2009. 702 p.
54. Rodrigues IDM. Processamento de compósitos cobre-grafite-alumina. 2013.
55. Aning AO, Wang Z, Courtney TH. Tungsten solution kinetics and amorphization of nickel in mechanically alloyed NiW alloys. Acta Metall Mater. 1993;41(1):165–74.
56. Wang GM, Campbell SJ, Calka A, Kaczmarek WA. Synthesis and structural evolution of tungsten carbide prepared by ball milling. J Mater Sci. 1997;32(6):1461–7.
57. Haruyama O, Asahi N. Amorphization of mixed Ni and Zr powders by mechanical alloying. J Alloys Compd. 1993;194(2):361–71.
58. El-Eskandarany MS. Controlling the powder milling process. Mechanical Alloying. 2015. 48–83 p.

59. M. S. EL-ESKANDARANY, K.Aoki K, Suzuki K. Rod Milling for Solid-State Formation of Al30Ta70 Amorphous Alloy Powder. 1990;167:113–8.
60. N. Cabrera ;, N. F. Mott. Theory of the oxidation of metals. Reports Prog Phys. 1949;12:163–84.
61. Platzman I, Brener R, Haick H, Tannenbaum R. Oxidation of Polycrystalline Copper Thin Films at Ambient Conditions. J Phys Chem C. 2008;112(4):1101–8.
62. Ammon C, Bayer A, Steinrück HP, Held G. Low-temperature partial dissociation of water on Cu(1 1 0). Chem Phys Lett. 2003;377(1–2):163–9.
63. Hodgson A, Haq S. Water adsorption and the wetting of metal surfaces. Surf Sci Rep. 2009;64(9):381–451.
64. McCormick GBSPG. Displacement Reactions during Mechanical Alloying. Metall Mater Trans A. 1990;21(October):2789–94.
65. H. Yang, G. Nguyen, P. G. McCormick. Mechanochemical Reduction of CuO by Graphite. Scr Metall &Materidia,. 1995;32(5):681–4.
66. Sheibani S, Ataie A, Khayati GR, Sheibani S, Ataie A, Khayati GR. Processing of nanocrystalline copper by mechanochemical reduction of CuO and Cu 2 O with graphite Processing of nanocrystalline copper by mechanochemical reduction of CuO and Cu 2 O with graphite. Mater Sci Technol. 2008;0836(May):986–90.
67. LIU L, Yuan Song-liu, Dong Yuan-da. Effect of Carbon Content on Mechanoreduction of Copper Oxide Effect of Carbon Content on Mechanoreduction of Copper Oxide. Chin Phys Lett. 1999;16(8).
68. Barin I. Thermochemical Data of Pure Substances. 1995.
69. Correia JB, Marques MT, Oliveira MM, Matteazzi P. Consolidation of dispersion strengthened nanostructured copper via hot extrusion. Mater Sci Forum. 2001;360–362:241–6.
70. Morris DG, Morris MA. Microstructure and strength of nanocrystalline copper alloy prepared by mechanical alloying. Acta Metall Mater. 1991;39(8):1763–70.
71. Van Trinh P, Bui HT, Tran BT, Van Tu N, Le DQ, Than XT, et al. The effect of sintering temperature on the mechanical properties of a Cu/CNT nanocomposite prepared via a powder metallurgy method. Adv Nat Sci Nanosci Nanotechnol. 2011;2(1).
72. Atkinson H V., Davies S. Fundamental aspects of hot isostatic pressing: An overview. Metall Mater Trans A Phys Metall Mater Sci. 2000;31(12):2981–3000.
73. Omori M. Sintering, consolidation, reaction and crystal growth by the spark plasma system (SPS). Mater Sci Eng A. 2000;287(2):183–8.
74. Saheb N, Iqbal Z, Khalil A, Hakeem AS, Al Aqeeli N, Laoui T, et al. Spark plasma sintering of metals and metal matrix nanocomposites: A review. J Nanomater. 2012;2012.
75. Nunes D, Livramento V, Correia JB, Hanada K, Carvalho PA, Mateus R, et al. Consolidation of Cu-nDiamond nanocomposites: Hot extrusion vs spark plasma sintering. Mater Sci Forum. 2010;636–637:682–7.
76. Miguel H, Cardoso V. Hardness modelling of porous copper bodies. Instituto Superior Técnico;

2017.
77. Rojac T, Kosec M, Malič B, Holc J. The application of a milling map in the mechanochemical synthesis of ceramic oxides. J Eur Ceram Soc. 2006;26(16):3711–6.
78. Jaeger HM, Nagel SR. Physics of the granular state. Science (80-). 1992;255(5051):1523–31.
79. Mojarrad NR, Kheirifard R, Mousavian RT, Afkham Y, Nakisa S. Filling ratio of vial: An important parameter for ball milling. J Therm Anal Calorim. 2016;126(3):1097–103.
80. B.D. C. Elements of X-ray Diffraction. Book. 1956. 84–85 p.
81. Fultz B, Howe J. Transmission Electron Microscopy and Diffractometry of Materials. 3rd ed. 2008.
82. Yoshio Waseda;Eiichiro Matsubara; Kozo Shinoda. X-ray Diffraction Crystallography. 2011.
83. Nelson JB, Riley DP. An experimental investigation of extrapolation methods in the derivation of accurate unit-cell dimensions of crystals. Proc Phys Soc. 1945;57(3):160–77.
84. Williamson GK, Hall WH. X-ray line broadening from filed aluminium and wolfram. Acta Metall. 1953;1(1):22–31.
85. Scardi P, Mccusker LB, Dreele RB Von, Cox DE, Loue D. Rietveld re ® nement guidelines. 1999;36–50.
86. Khitouni M, Daly R, Mhadhbi M, Kolsi A. Structural evolution in nanocrystalline Cu obtained by high-energy mechanical milling: Phases formation of copper oxides. J Alloys Compd. 2009;475(1–2):581–6.
87. Speakman S. Introduction to X-Ray Powder Diffraction Data Analysis. Center for Materials Science and Engineering at MIT.
88. Goldstein JI, Newbury DE, Echlin P, Joy DC, Fiori C, Lifshin E, et al. Scanning electron microscopy and X-ray microanalysis: a text for biologists, materials scientists, and geologists. Scanning Electron Microscopy and X-Ray Microanalysis. 1981. 205–273 p.
89. Hassing S. What Is Vibrational Raman Spectroscopy: A Vibrational or an Electronic Spectroscopic Technique or Both? Mod Spectrosc Tech Appl. 2020;1–25.
90. Brown JRFKNCW. Introductory Raman Spectroscopy. 2nd ed. Vol. 4, EMBO Reports. Elsevier; 2003. 1–94 p.
91. Tuinstra F, Koenig JL. Raman Spectrum of Graphite. J Chem Phys. 1970;53(3):1126–30.
92. Cançado LG, Pimenta MA, Saito R, Jorio A, Ladeira LO, Grueneis A, et al. Stokes and anti-Stokes double resonance Raman scattering in two-dimensional graphite. Phys Rev B - Condens Matter Mater Phys. 2002;66(3):354151–5.
93. Bogas JA, Hawreen A, Olhero S, Ferro AC, Guedes M. Selection of dispersants for stabilization of unfunctionalized carbon nanotubes in high pH aqueous suspensions: Application to cementitious matrices. Appl Surf Sci. 2019;463(July):169–81.
94. Schwan J, Ulrich S, Batori V, Ehrhardt H, Silva SRP. Raman spectroscopy on amorphous carbon films. J Appl Phys. 1996;80(1):440–7.
95. Welham NJ, Berbenni V, Chapman PG. Effect of extended ball milling on graphite. J Alloys Compd. 2003;349(1–2):255–63.

96. Maslova OA, Ammar MR, Guimbretière G, Rouzaud JN, Simon P. Determination of crystallite size in polished graphitized carbon by Raman spectroscopy. Phys Rev B - Condens Matter Mater Phys. 2012;86(13):1–5.
97. Hryha E, Zubko P, Dudrová E, Pešek L, Bengtsson S. An application of universal hardness test to metal powder particles. J Mater Process Technol. 2009;209(5):2377–85.
98. Milman Y V., Golubenko AA, Dub SN. Indentation size effect in nanohardness. Acta Mater. 2011;59(20):7480–7.
99. Nix WD, Gao H. Indentation size effects in crystalline materials: A law for strain gradient plasticity. J Mech Phys Solids. 1998;46(3):411–25.
100. Manika I, Maniks J. Size effects in micro- and nanoscale indentation. Acta Mater. 2006;54(8):2049–56.
101. Abu Al-Rub RK. Prediction of micro and nanoindentation size effect from conical or pyramidal indentation. Mech Mater. 2007;39(8):787–802.
102. Qiao XG, Starink MJ, Gao N. The influence of indenter tip rounding on the indentation size effect. Acta Mater. 2010;58(10):3690–700.
103. McElhaney KW, Vlassak JJ, Nix WD. Determination of indenter tip geometry and indentation contact area for depth-sensing indentation experiments. J Mater Res. 1998;13(5):1300–6.
104. Kareer A, Hou XD, Jennett NM, Hainsworth S V. The interaction between Lateral size effect and grain size when scratching polycrystalline copper using a Berkovich indenter. Philos Mag. 2016;96(32–34):3414–29.
105. Hou X, Jennett NM. Application of a modified slip-distance theory to the indentation of single-crystal and polycrystalline copper to model the interactions between indentation size and structure size effects. Acta Mater. 2012;60(10):4128–35.
106. Oliver WC, Pharr GM. Measurement of hardness and elastic modulus by instrumented indentation: Advances in understanding and refinements to methodology. J Mater Res. 2004;19(1):3–20.
107. Ivan Diogo Mendonça Rodrigues. Processamento de compósitos cobre-grafite-alumina. Instituto Superior Técnico; 2013.
108. Madavali B, Lee JH, Lee JK, Cho KY, Challapalli S, Hong SJ. Effects of atmosphere and milling time on the coarsening of copper powders during mechanical milling. Powder Technol. 2014;256:251–6.
109. Shukla AK, Nayan N, Murty SVSN, Mondal K, Sharma SC, George KM, et al. Processing copper-carbon nanotube composite powders by high energy milling. Mater Charact. 2013;84:58–66.
110. Zhang DL, Raynova S, Koch CC, Scattergood RO, Youssef KM. Consolidation of a Cu-2.5 vol.% Al2O3 powder using high energy mechanical milling. Mater Sci Eng A. 2005;410–411:375–80.
111. Seixas T. Development and modeling of mechanical alloying for production of copper matrix composite powders reinforced with alumina and graphite. Instituto Superior Técnico; 2016.
112. Hellstern E, Fecht HJ, Fu Z, Johnson WL. Structural and thermodynamic properties of heavily mechanically deformed Ru and AlRu. J Appl Phys. 1989;65(1):305–10.

113. Eckert J, Holzer JC, Krill CE, Johnson WL. Mechanically driven alloying and grain size changes in nanocrystalline Fe-Cu powders. J Appl Phys. 1993;73(6):2794–802.
114. Nunes D. Carbon dispersions in nanostructured metals. Instituto Superior Técnico; 2012.
115. Marques MT, Correia JB, Conde O. Carbon solubility in nanostructured copper. Scr Mater. 2004;50(7):963–7.
116. Eckert J, Holzer JC, Krill CE, Johnson WL. Reversible grain size changes in ball-milled nanocrystalline Fe—Cu alloys. J Mater Res. 1992;7(8):1980–3.
117. Kim WJ, Park IB, Han SH. Formation of a nanocomposite-like microstructure in Mg-6Al-1Zn alloy. Scr Mater. 2012;66(8):590–3.
118. Thompson JG. Effects of cold-rolling on the indentation hardness of copper. J Res Natl Bur Stand (1934). 1934;13(5):745.
119. Gupta S, Singh G. a Review on Fabrication of Copper Graphite Composite Material & Its Mechanical Properties. Ijariie. 2016;2(5):594–9.
120. Taha AS, Hammad FH. Application of the Hall-Petch Relation to Microhardness Measurements on Al, Cu, Al-MD 105, and Al-Cu Alloys. Phys Status Solidi. 1990;119(2):455–62.